Schweizerische Eidgenossenschaft
Confédération suisse
Confederazione Svizzera
Confederaziun svizra

Department of the Environment,
Transport, Energy and Communication DETEC

Swiss Federal Office of Energy SFOE
Energy Research

Final report

PECHouse 3

Photoelectrochemical water splitting for solar production of hydrogen

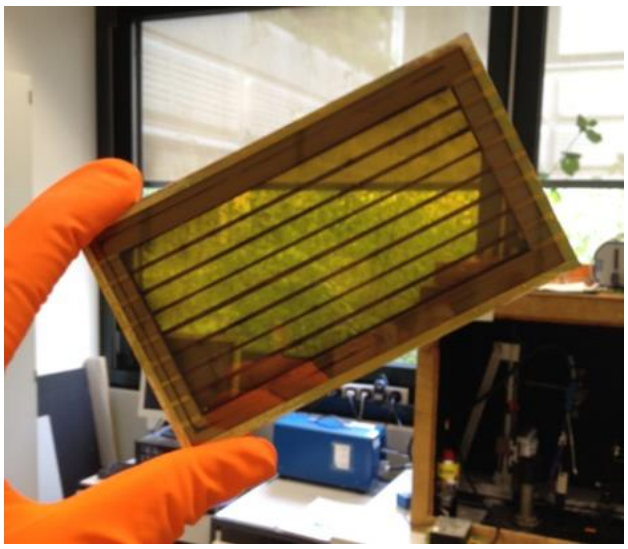

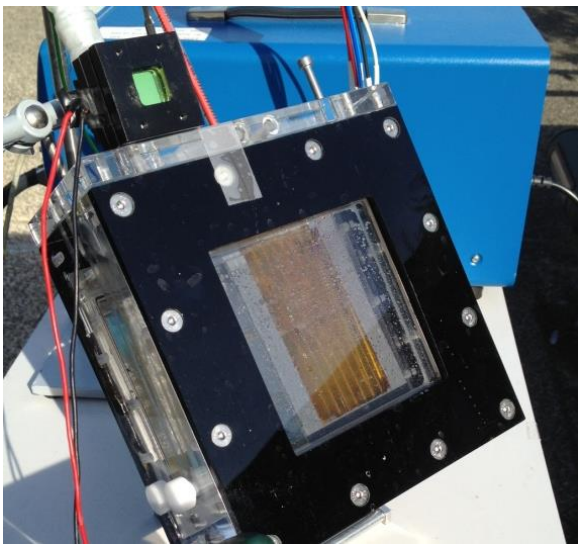

Date: 22 December 2017

Place: Lausanne

Publisher:
Swiss Federal Office of Energy SFOE
Research Programme Hydrogen
CH-3003 Bern
www.bfe.admin.ch
energieforschung@bfe.admin.ch

Agent:
Ecole polytechnique fédérale de Lausanne
Laboratory of Photonics and Interfaces
EPFL ISIC LPI, Station 6
CH-1015 Lausanne
http://lpi.epfl.ch

Author:
Jingshan Luo, EPFL, jingshan.luo@epfl.ch
Michael Grätzel, EPFL, michael.graetzel@epfl.ch
David Bernhardsgrütter, ZHAW, bens@zhaw.ch
Jürgen Schumacher, ZHAW, schm@zhaw.ch
Romain Carron, EMPA, romain.carron@empa.ch
Ayodhya Tiwari, EMPA, ayodhya.tiwari@empa.ch

SFOE head of domain: Stefan Oberholzer, stefan.oberholzer@bfe.admin.ch
SFOE programme manager: Stefan Oberholzer, stefan.oberholzer@bfe.admin.ch
SFOE contract number: SI/500090-03

Summary

The significant progress of the PECHouse3 project includes the advancement of Cu_2O photocathodes, exploration of new p-type Cu2S materials, modelling of optoelectronic processes, and demonstration of a variety of tandem configurations for standalone sunlight-driven water splitting.

The photoelectrochemical (PEC) performance of Cu_2O photocathodes was boosted to 10 mA cm-2 at 0 V versus reversible hydrogen electrode (RHE) with an onset potential of 1 V versus RHE by marrying the buried Cu_2O/Ga_2O_3 heterojunction with nanowire structured electrode, which is by far the best metal oxide based photoelectrode for solar water splitting. In addition, solution processed Cu_2S photocathodes were developed, achieving a photocurrent density up to 7.0 mA cm-2 at -0.3 V versus RHE under AM 1.5G simulated sunlight illumination. Optoelectronic models were created to understand and optimize photoelectrode device architectures in terms of composition, doping, and morphology.

In the end, we demonstrated two types of standalone tandem solar water splitting devices. One is composed of perovskite light harvesters, Earth-abundant catalysts and a bipolar membrane. Overall, 10 mA cm-2 current density with 1.63 V bias voltage for electrochemical water splitting and 12.7% solar to hydrogen conversion efficiency for solar driven water splitting were achieved. The second is an all oxide based tandem, composed of a Cu_2O photocathode and a $BiVO_4$ photoanode, and 3% STH conversion efficiency was achieved. Furthermore, we showed the scale up possibility using Cu_2O photocathodes as an example.

Contents

List of abbreviations

APCE	absorbed photon-to-current efficiency
ALD	atomic layer deposition
AM1.5G	global standard spectrum of the sun
AZO	Al-doped zinc oxide
BER	back electron-hole recombination
CB	conduction band
CBO	conduction band offset
EC	equivalent circuit
EE	relates to illumination from the front side
EIS	electrical impedance spectroscopy
HJ	heterojunction
HER	hydrogen evolution reaction
IPCE	incident photon-to-current conversion efficiency
IV	current voltage
LB	Lambert-Beer
NW	nanowire
OM	optical model
OER	oxygen evolution reaction
PEC	photoelectrochemical cell
RHE	reversible hydrogen electrode
SRH	Shockley Read Hall
SEI	semiconductor-electrolyte interface
SCLJ	semiconductor/liquid junction
STH	solar to hydrogen
XPS	X-ray photoelectron spectroscopy

1 Introduction

It is necessary to develop renewable energy resources as we move away from traditional fossil fuels and nuclear energy. Energy from sunlight represents the largest and most promising source, but its intermittent nature makes it difficult to implement on a large scale. Our energy demand, however, is not intermittent, so a method of efficiently storing and transporting its energy will be crucial. The electric grid suffers significant efficiency losses at long distances. Batteries are heavy and expen-sive and thus are not ideal for energy transport. The conversion and storage of solar energy into chemical fuels therefore represents an important goal.

In the quest to develop a sustainable energy economy, the utilization of solar energy to generate clean fuel represents the ultimate goal. Hydrogen (H_2) is a leading candidate for a carbon-neutral fuel, and its production by photoelectrochemical (PEC) splitting of water is a promising route for sustainable fuel generation. Hydrogen is an immense commercial commodity worldwide, not only as fuel but also as a crucial feedstock in the chemical industry. Its widespread production from renewable sunlight may enable its implementation as a chemical fuel, provided it can be accomplished at low costs to be competitive with traditional fossil fuels. The clean and renewable nature of hydrogen is a major advantage over fossil fuels, since it can be produced from abundant water and when con-sumed (by combustion or in a fuel cell) releases water as its only emission.

A solar-driven electrolysis system must be inexpensive and composed of abundant and scalable materials in order to compete with conventional means of hydrogen generation. At present, the cou-pling of commercial photovoltaic (PV) and electrolyzer modules remains too expensive to compete with other forms of H_2 production. PEC hydrogen production has the potential to compete with the combined PV and electrolyzer approach. This would require, by some estimates, solar-to-hydrogen (STH) efficiencies of at least 10%, a theoretically achievable but challenging goal when limited to inexpensive materials and processes. In PECHouse3 we will push PEC hydrogen production toward this efficiency goal in an effort to prove that the technology is a viable route to renewable energy harvesting.

2 Context

The achievements of the projects “PECHouse2” and “NanoPEC” included significant progress toward cost-effective PEC-based water splitting. At EPFL-LPI, research on metal oxide semiconductors has identified Cu_2O and Fe_2O_3 as promising photoelectrode materials toward achieving the efficiency goals. Both are cheap and abundant materials and possess theoretical STH efficiencies exceeding 16%. To approach the elusive 10% mark, we have studied numerous design principles for improving photoelectrode performance. The general goals are to enhance photocurrents (corresponding to the rate of H_2 generation) and improve photovoltages (providing a larger driving force toward the elec-trolysis reaction).

For the photocathode efforts, we developed p-n junctions between Cu_2O and n-type metal oxide over-layers which provide strong photovoltage toward water reduction. Coupling with H_2 evolution cata-lysts RuO_2 or MoS_2 yielded device photocurrents that would correspond with STH efficiencies over 6% in a tandem configuration. To further advance the Cu_2O photocathode, we propose clear directions toward improving both the photocurrent and photovoltage of the device. The severe drop in spectral response to photon wavelengths beyond 500 nm is evidence of a poor absorption coefficient in that range, which we will address by incorporating light management strategies such as back reflectors. The device performance will be improved by increasing the Cu_2O conductivity through controlled doping.

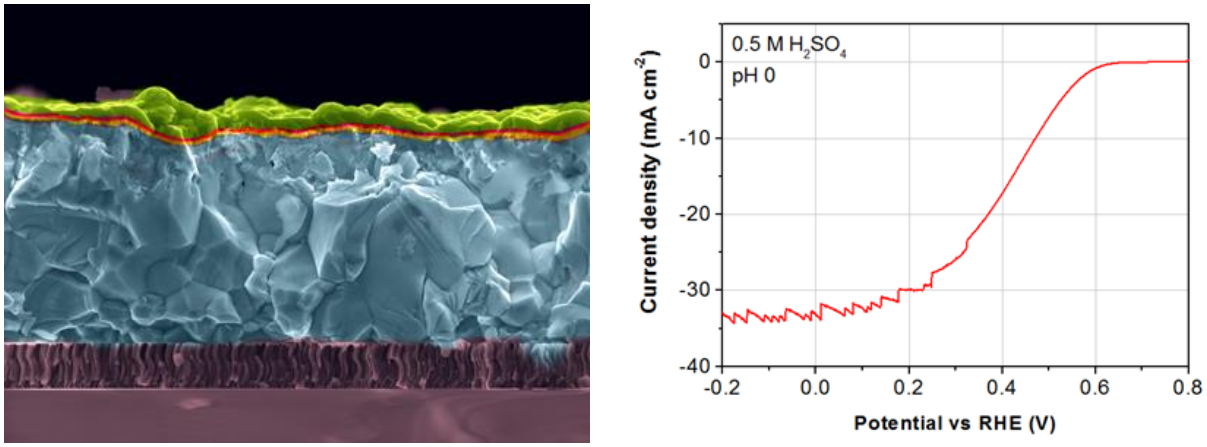

CIGS photocathode. Left: cross section microscopy image of the device (FTO/glass, CIGS, CdS, i:ZnO, TiO2). Right: photocathode response in pH 0 water under simulated sunlight il-lumination..

To enhance the photovoltage toward 0.8-1.0 V which should be possible on Cu_2O, we will explore different metal oxide contacting layers to improve the p-n junction behavior beyond the current state-of-the-art.

Our group has recently demonstrated a new candidate photocathode device based on the photovoltaic material Cu(In,Ga)Se_2 (CIGS). These materials developed by EMPA-TFP were treated with the ALD overlayers typical of the Cu2O photocathode approach, and the resulting devices were found to exhibit excellent performance toward PEC hydrogen evolution. The enhanced photocurrents result from a combination of the smaller bandgap of CIGS and its high quantum efficiencies for charge generation. Furthermore, the photovoltage we observed was already competitive with that achieved on optimized Cu_2O devices. Further study of CIGS-based PEC systems is therefore an important direction that will be pursued in PECHouse3.

For the photoanode approach, the record photocurrent Fe_2O_3 nanostructure devices, developed by our group, have shown us the importance of introducing and controlling the fine structure and doping of the Fe_2O_3 material. To further advance iron oxide, we have recently developed an ad-vanced home-built atomic layer deposition (ALD) system capable of depositing thin films of Fe_2O_3 onto high aspect ratio conductive scaffolds. By this route we target improved light absorption and carrier collection to yield photocurrent enhancements beyond the ~4.0 mA/cm^2 record. This photocurrent enhancement will be achieved by employing host-guest architectures where thin Fe_2O_3 films are deposited onto conductive nanostructures, as shown below. The ALD will importantly also allow us to explore the p–n junction approach toward higher photovoltages by depositing thin p-type metal oxide films onto Fe_2O_3. Making p-type metal oxides is notoriously difficult, but the fine composition control of ALD will allow us to explore the deposition of various ternary compounds, from doped Fe_2O_3 to metal ferrites ($CuFe_2O_4$, $NiFe_2O_4$).

The physical phenomena of light absorption and charge transport in metal oxide photoelectrodes were investigated by means of model-based numerical simulations at ICP ZHAW during the PECHouse2 project. The calculated photocurrent-voltage dependency reveals recombination losses previously not accounted for by the analytical models. The calculation of the energy band diagram of photoelectrodes can now be done quantitatively for different materials. We are working toward numerical simulation of photoelectrochemical impedance spectroscopy (PEIS) measurements, which will enable accurate verification of our model with measurement data for charge transfer from valence band or surface states. Further development of our physical model is needed to increase the photocurrent (suppress recombination losses) and the photovoltage (internal p–n junctions) of the photoelectrodes.

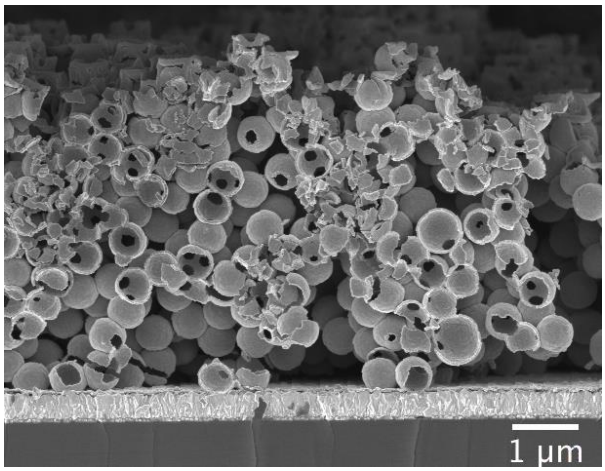

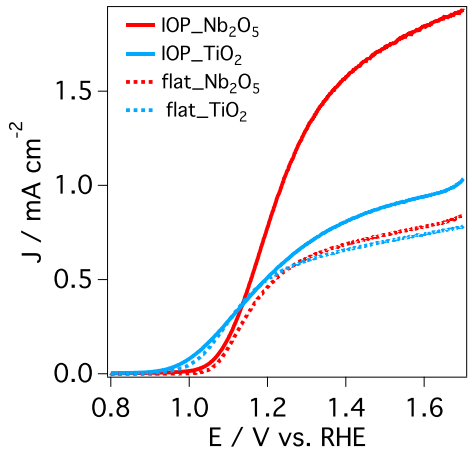

Fe_2O_3 host-guest photoanode. Left: Nb:SnO_2 conductive scaffold with conformal thin coat-ing of ALD Fe_2O_3. Right: Photoanode response of flat and host-guest architectures.

Recombination processes and rates can be probed by PEIS and transient absorption spectroscopy (TAS). Measurements and simulations of open-circuit potential (OCP) of the photoelectrode will be used to understand the low photovoltage. Working closely together, the groups at EPFL and ZHAW will acquire data by these experimental techniques and use them to develop models to predict the key parameters in the system (doping, geometry, conductivity, etc.) that must be addressed in the devices.

No single-absorber photoelectrode system can drive efficient sunlight-driven water splitting itself, as the relationship between band gap and spectral sensitivity precludes achieving simultaneously the high voltage and high photocurrent needed for appreciable rates of hydrogen production. Instead, a multiple-absorber system is necessary, comprising two or more light absorbing components of different band gaps. Our primary target configuration is to couple a PEC photoelectrode with a low-cost photovoltaic (PV) component in an architecture deemed a PEC-PV tandem. This constitutes a multiple-absorber system which allows more efficient utilization of the solar spectrum, wherein the wider-bandgap metal oxide photoelectrode absorbs the higher-energy photons while the PV component utilizes the lower-energy photons to generate the necessary additional photovoltage. This has been demonstrated at moderate efficiency by EPFL-LPI using photoanodes coupled to dye-sensitized PV cells. In this project, with the goal of a demonstrable PEC-PV tandem, we will work primarily with commercial or near-commercial technologies. We are in collaboration with the photovoltaics group of Prof. Christophe Ballif (EPFL) as well as our PECDEMO partners from Helmholtz-Zentrum Berlin to design and produce silicon-based PV modules for this purpose. Additionally, from our recent successes using high-voltage hybrid perovskite PVs toward water splitting, these emerging devices will be explored for the PEC-PV tandem application.

2.1 Goals

Our design for an efficient PEC-PV device requires a wavelength-selective dichroic mirror to split the incident solar spectrum. The general configuration entails placing the photovoltaic cell in the path of direct sunlight illumination, then inserting the dichroic mirror across the light path at a 45° angle, thereby reflecting the higher-energy photons perpendicularly onto the photoelectrode device as shown in the schematic below. This approach has several advantages. The wavelength cutoff can be selected (by mirror design) to selectively reflect and transmit the desired wavelength ranges to balance the photocurrent outputs of the PV and PEC components. Use of a mirror allows spatial

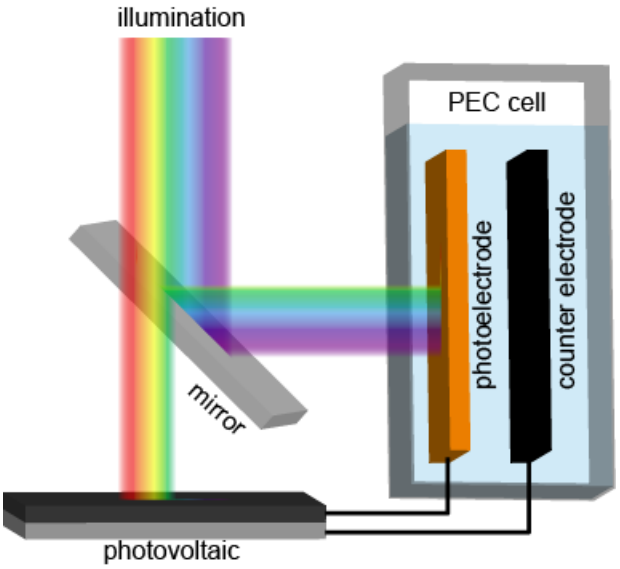

Fe_2O_3 host-guest photoanode. Left: Nb:SnO_2 conductive scaffold with conformal thin coat-ing of ALD Fe_2O_3. Right: Photoanode response of flat and host-guest architectures.

separation of the two components, keeping the PV away from the possibly corrosive electrolyte and allowing easier diagnostics and maintenance of the individual components. Additionally, by splitting the spectrum, we are not limited to using transparent photoelectrodes, greatly broadening the device design options. Importantly, the efficiency of such a device is determined by considering the area of direct incident sunlight onto the mirror, giving us the best chance at high efficiencies from a compact device.

While the ultimate goal of solar to H_2 fuel conversion may be utility-scale power plants, an initial important application for PEC-PV modules is for local fuel generation at private homes or locations isolated from the electricity grid. To this end, a prototype module capable of producing H_2 could be used to demonstrate local solar fuel production. Scale-up of these test devices to more meaningful dimensions will require adapting of the synthetic methods and cell design, but the knowledge gained by the smaller prototype studies should transfer directly to the scale-up efforts. A goal of the present project will be to demonstrate the scalability of the technology by producing a PEC-PV device comprising a modular combination of four 50 cm^2 (7.1 cm x 7.1 cm) devices in a 2x2 array, capable of stable operation at 10% solar-to-hydrogen efficiency.

In a parallel effort, an advanced tandem photovoltaic will be designed specifically for PV-driven electrolysis. The initial result of using two series-connected perovskite photovoltaics already achieved over 12% STH efficiency, despite using a side-by-side PV configuration which doubled the illuminated area (thereby halving the efficiency).(*17*) A tandem approach with two different light absorbers, as described above, can produce even higher efficiencies. We will seek to maximize the STH efficiency using a PV tandem between a perovskite top cell and silicon or CIGS bottom cell. At the end of the project we will assess and compare the different approaches toward complete water splitting, in terms of efficiency, cost, abundance, and simplicity.

In summary, the PECHouse3 project will further advance metal oxide-based photoelectrodes while also exploring the potential of CIGS, and ultimately create a high-performance PEC-PV device for standalone hydrogen production. Although impressive progress has already been made with these materials, there remain important challenges to address in order to realize their full potential. Notably, the photovoltage of each needs to be enhanced to yield improved STH efficiency. The ALD technique

will allow us to explore more promising junction materials, including Ga_2O_3 for the Cu_2O electrode, and p-type metal oxides as overlayers for the Fe_2O_3 electrode. Additionally, voltage gains in the PV component can improve the photocurrent of the full device. New developments in high-V_{oc} perovskite PVs will be utilized in the optimization of PEC-PV tandems, as well as application in photovoltaic tandems, with the goal of demonstrating high STH efficiencies.

The goals for the continuation of the PECHouse project include development of more efficient photoelectrodes, coupling photoelectrodes with photovoltaics in PEC-PV tandems that perform unbiased water splitting at current densities exceeding 8 mA/cm^2, comparing this approach with photovoltaic-based tandem electrolysis configurations, and development of a demonstration-scale modular device of 200 cm^2 illuminated area that performs unbiased water splitting.

3 Photoelectrode development (WP1)

3.1 Cu_2O photocathode

Due to its abundance, scalability, and nontoxicity, Cu_2O has attracted extensive attention toward solar energy conversion, and it is today's best performing metal oxide material. With a band gap of 2.0 eV, Cu_2O could theoretically deliver a solar to hydrogen conversion efficiency of 18% for water splitting and a power conversion efficiency of 20% as a solar cell.

3.1.1 Nanowire structure toward higher photocurrent density

One of the challenges of Cu_2O for solar water splitting is its unfavorable ratio of the carrier diffusion length over the light absorption depth. In order to efficiently absorb sunlight, Cu_2O films must typically be at least 1 µm thick. However, the minority carrier (electron) diffusion length is limited to about 200 nm or less, depending on the synthetic method. This results in inefficient collection of photogenerated carriers. Even though various attempts have been made to enhance the carrier collection in Cu_2O, including doping, high temperature processing, and overlayer engineering, the photocurrent density still remains low for this material. Nanostructured photoelectrodes, especially nanowire (NW) arrays, constitute an attractive approach to solve this problem through morphology control, combining efficient light harvesting along the full length of the wire with short radial diffusion distance for the minority carriers toward the electrolyte solution. Furthermore, nanostructures offer a large surface area, leading to increased exposure of catalytic sites and accelerated reaction kinetics. In this project, we developed a new synthetic method to grow Cu_2O nanowire arrays on conductive fluorine-doped tin oxide substrates with well-controlled phase and excellent electronic and photonic properties. Also, we introduced an innovative blocking layer strategy to enable high performance. Further, through material engineering by combining a conformal nanoscale p–n junction, durable protective overlayer, and uniform catalyst decoration, we have successfully fabricated Cu_2O nanowire array photocathodes for hydrogen generation from solar water splitting delivering unprecedentedly high photocurrent densities of 10 mA cm^{-2} and stable operation beyond 50 h, establishing a new benchmark for metal oxide based photoelectrodes (Figure 1).

3.1.2 Ga_2O_3 buffer layer toward higher photovoltage

Though nanowire structure can elevate the photocurrent density of Cu_2O electrodes. However, the shortcoming of low photovoltage still needs to be addressed for efficient water splitting. In a Cu_2O heterojunction device, the photovoltage is determined by the Fermi level difference between Cu_2O and the buffer layer, so choosing an appropriate buffer layer is crucial for achieving high photovoltages.

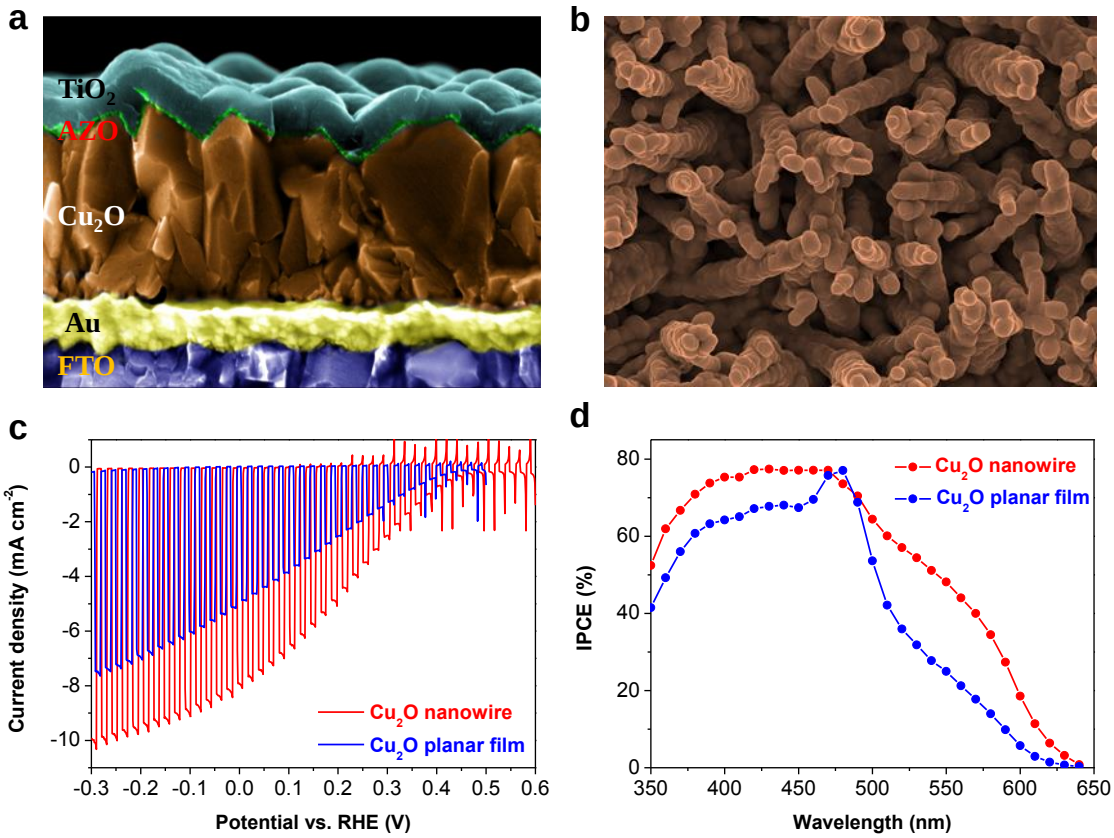

Figure 1: a, SEM image of planar Cu_2O photoelectrode. b, SEM image of nanowire structure Cu_2O photoelectrode. c, J–V curves of Cu_2O photoelectrodes under simulated AM 1.5G chopped illumination. d, IPCE spectra under monochromatic illumination of Cu_2O photoelectrodes.

Thus, in the following, we rationally choose Ga_2O_3 as a new buffer layer for Cu_2O photoelectrodes. Compared to the conventional AZO buffer layer, Ga_2O_3 has a much higher conduction band level, resulting in better band alignment with Cu_2O decreasing the conduction band discontinuity. We illustrated the band energy level alignments of Cu_2O/AZO and Cu_2O/Ga_2O3 in detail using X-ray photoelectron spectroscopy and UV-vis absorption spectroscopy (Figure 2a and b). Experimentally, compared to the device with AZO buffer layer, the electrode with Ga_2O_3 shows a 0.5 V anodic shift in onset potential, in agreement with the conduction band energy level difference between AZO and Ga_2O_3. Remarkably, at 0.5 V vs. RHE, the sample with the Ga_2O_3 buffer layer already delivers a photocurrent density of 6.5 mA cm^{-2}, which is just the onset for the sample with AZO. Moreover, at 0 V vs. RHE, current density reaches 10 mA cm^{-2} (Figure 2c).

3.1.3 NiMo catalyst toward stable operation in alkaline electrolyte

In order to realize efficient and long-term water splitting, a strong acid or base electrolyte has to be used to increase the conductivity and minimize the pH gradient that arises from the proton consumption at the cathode and proton production at the anode. In addition, as most of the Earth-abundant electrocatalysts for the oxygen evolution reaction (OER) operate in alkaline electrolytes, and tandem devices are imperative for maximizing the utilization of sunlight and driving complete water splitting, it is essential to design our photocathodes to operate in alkaline working environments. Thus, in the next step, we try to develop Cu_2O photoelectrodes with stable operation in alkaline condition.

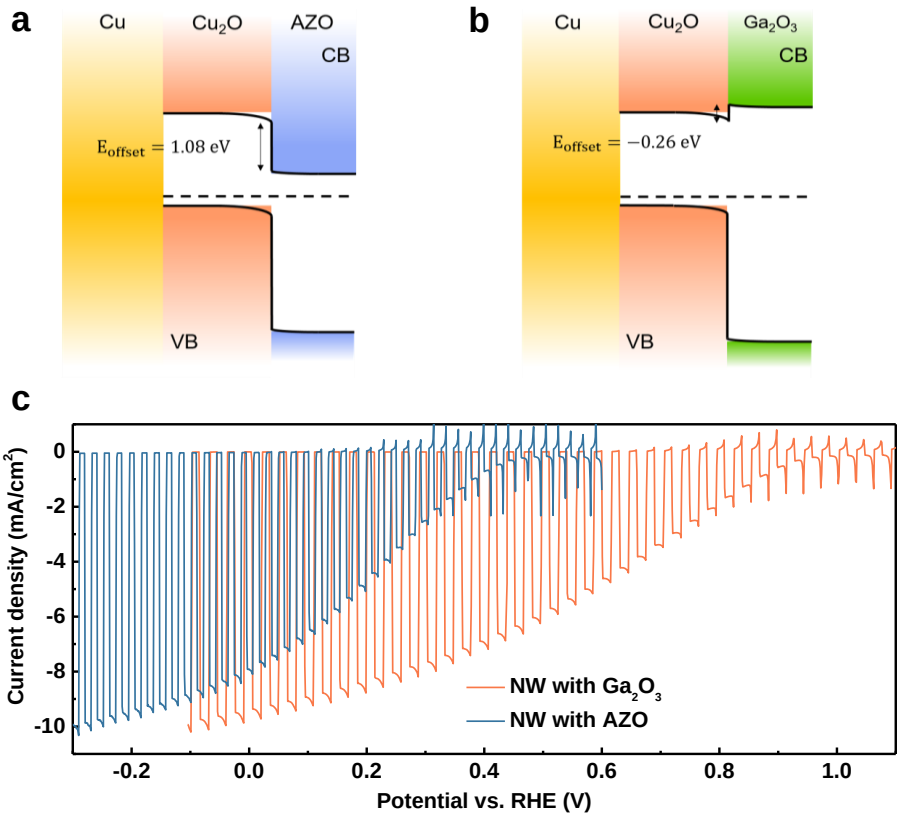

Figure 2: a, Cu_2O/AZO and b, Cu_2O/Ga_2O_3 heterojunctions with different conduction band offsets assuming pinning of the band edges of the semiconductors at the interfaces. c, J-E response under simulated one sun AM 1.5G chopped illumination for Cu_2O nanowire photocathodes with AZO and Ga_2O_3.

RuO_x as a hydrogen evolution catalyst is not stable for alkaline electrolyte, so we chose NiMo as the electrocatalyst for our electrode, which showed remarkable activity and stability in alkaline electrolytes. We photo-electrodeposited NiMo onto Cu_2O NW photoelectrodes. After deposition, the morphology of the electrode was well preserved (Figure 3). The current density for the NiMo modified photocathode reaches 8.2 mA cm^{-2} at 0 V vs. RHE, which is comparable to that of the RuO_x modified sample (Figure 4a). The long-term stability of NiMo modified Cu_2O NW photoelectrodes in alkaline electrolyte was evaluated under continuous AM 1.5G illumination at 0.5 V vs. RHE (Figure 4b). After 8 h, the current density retained ~90% of its maximum value. Considering the excellent stability of NiMo as an electrocatalyst in alkaline electrolyte, the decrease is probably due to the degradation caused by electrolyte penetration into the amorphous TiO_2 layer.

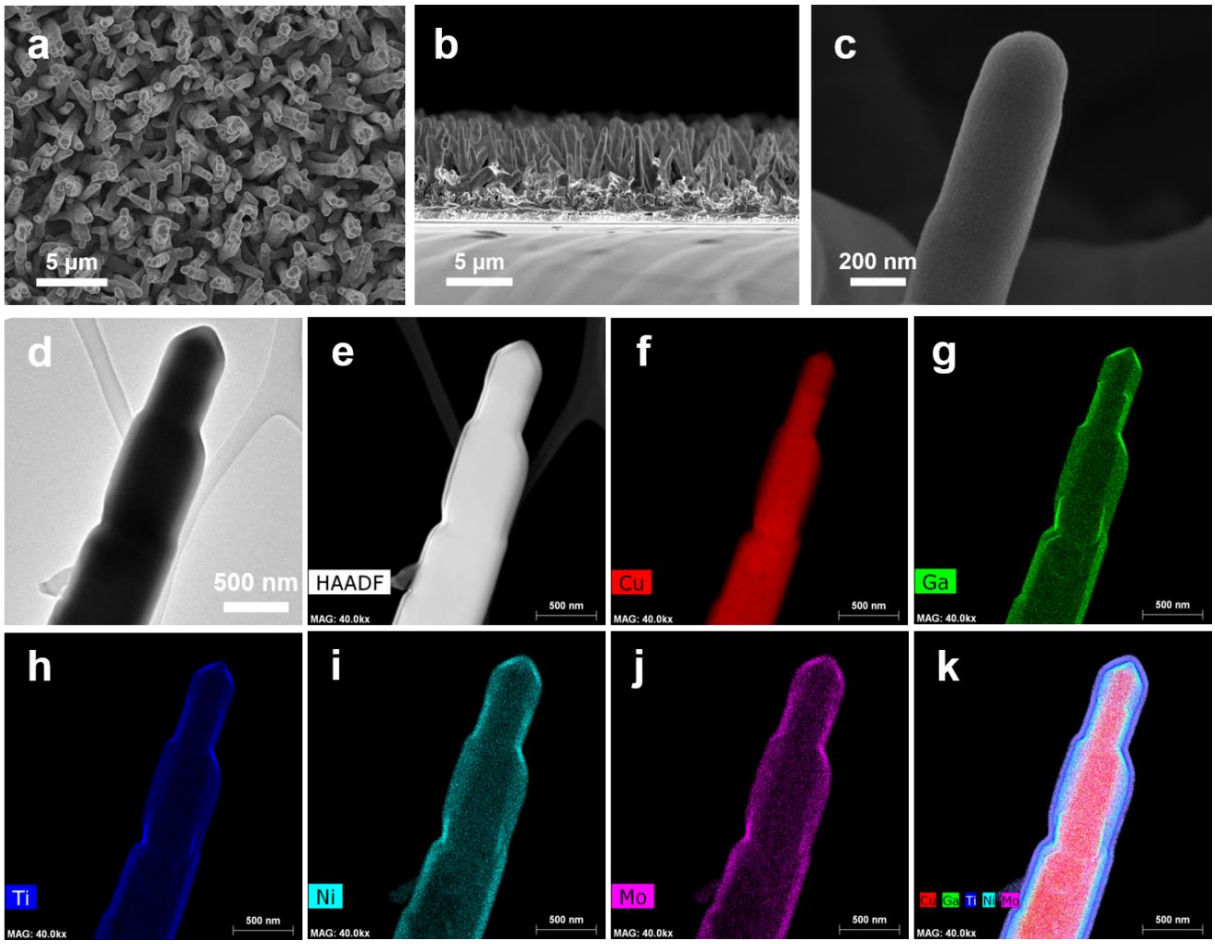

Figure 3: Electron microscopy of NiMo modified Cu_2O photocathodes. a, Top view SEM image of NiMo coated Cu_2O nanowire photocathodes. b, Cross-section image of cleaved Cu_2O photocathodes. c, Magnified SEM image focused on a single nanowire. d, High resolution transmission electron micrograph of Cu_2O NW photoelectrode. e, High-angle annular dark-field (HAADF) image of Cu_2O NW photoelectrode. f-j, Elemental mapping images of Cu, Ga, Ti, Ni and Mo, respectively. k, Combined elemental mapping image of Cu Ga, Ti, Ni and Mo.

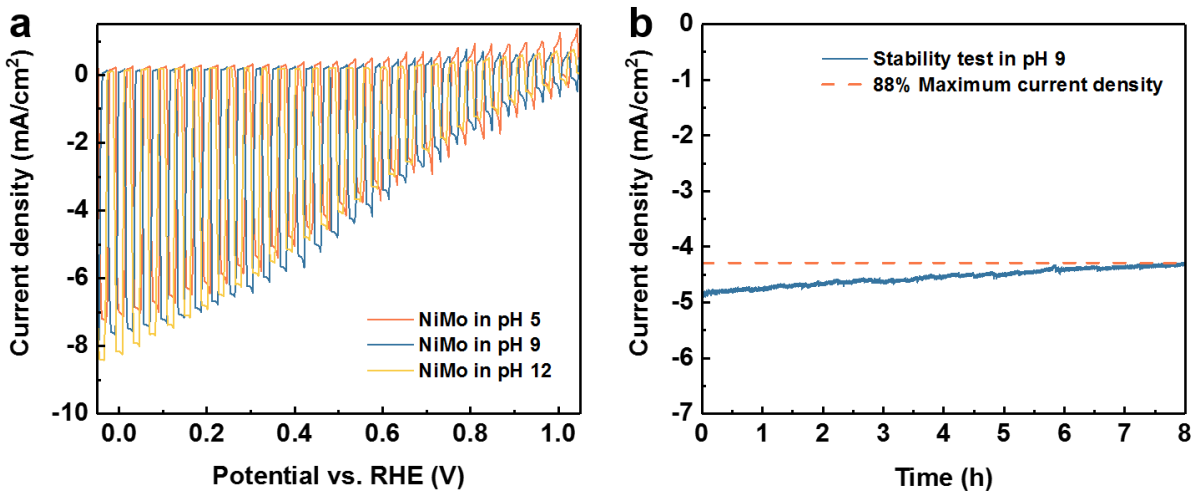

Figure 4: Photoelectrochemical measurement on NiMo modified Cu_2O photocathodes. a, J-E response under simulated AM 1.5G chopped illumination in different pH buffer solutions. b, Chronopotentiometry measurement on NiMo modified Cu_2O photocathode in pH 5 buffer solution with continuous illumination and stirring.

3.1.4 Light management strategies

One key deficiency of our previously-demonstrated Cu_2O–perovskite tandem (Dias *et al., Advanced Energy Materials* 2015) was the poor transparency of the Cu_2O photocathode to long-wavelength photons which must pass through to illuminate the perovskite cell. One culprit was the semi-transparent gold substrate layer that was necessary for successful Cu_2O electrodeposition. We therefore sought to identify a more transparent substrate layer that could be used, and we decided to attempt the use of wide band gap p-type nickel oxide. Seemingly due to low conductivity, dense films of Cu_2O would not deposit onto the bare nickel oxide. We then incorporated Cu as a dopant, yielding thin films of mixed copper-nickel oxide. These films were deposited onto FTO-glass substrates followed by Cu_2O electrodeposition, which worked well in this case. Completing the device by ALD overlayers and catalyst deposition, the resulting photocathodes were notably more transparent. As shown in Figure 5a, the devices based on CuO/NiO substrates had up to 20% improvement in transparency out to 800 nm wavelength, due to the wide band gap nature of NiO. This will be key for light management in the device, enabling strong illumination of the second absorber. Along with the improved transparency, the devices also showed improved photocathode activity, Figure 5b. Across the spectrum, the IPCE response was improved (Figure 5c), suggesting that charge extraction was more efficient when CuO/NiO underlayers were used. Since it is a wide band gap p-type oxide, we believe that NiO is able to act as a blocking layer to avoid back recombination of conduction band electrons in Cu_2O, as shown in Figure 5d. This resulted in higher current densities than for samples using Au underlayers. Furthermore, this configuration avoided the use of the noble metal Au, bringing us one step closer to an all earth-abundant water splitting device.

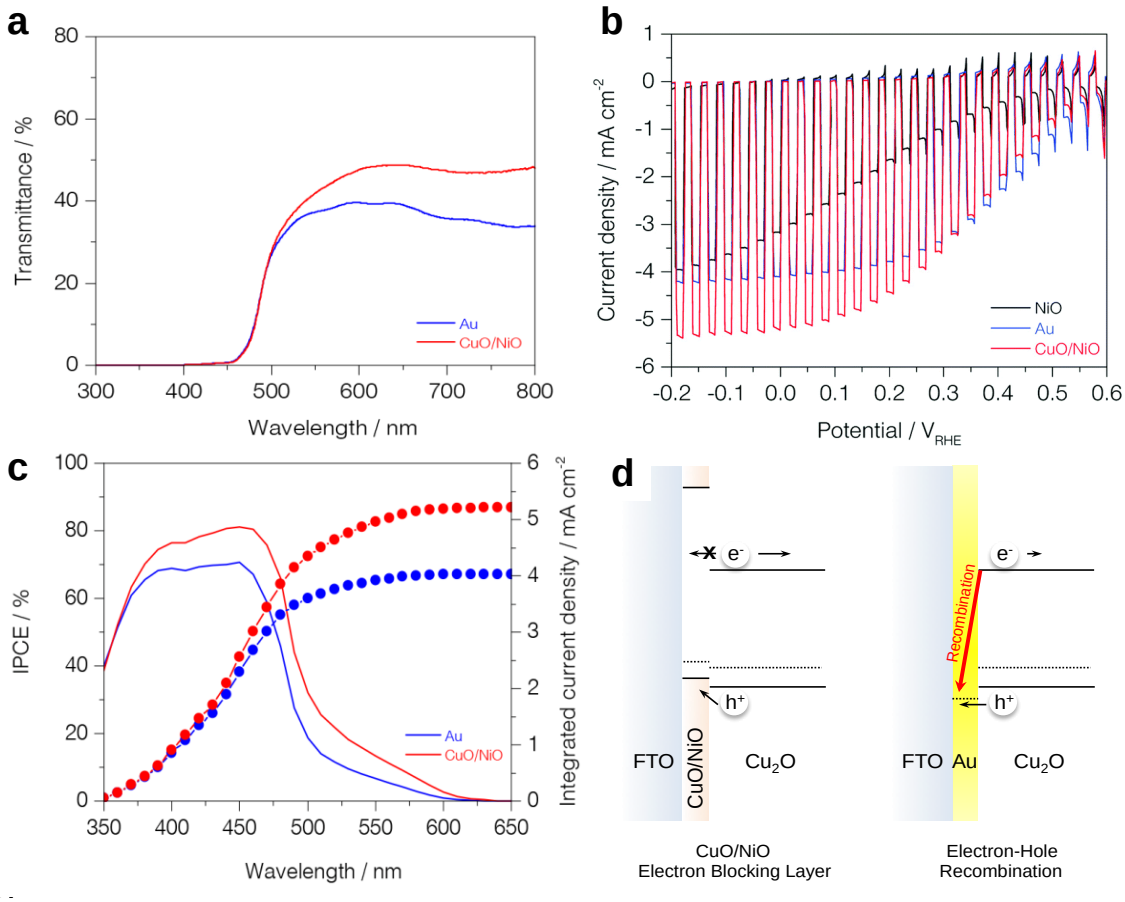

Figure 5: CuO/NiO substrate-based Cu_2O photocathodes. a, Device transmittance spectra. b, J–V characteristics of Cu_2O photocathodes on 4 nm thick NiO (black), 3 nm thick Au (blue) and 4.4 nm CuO/NiO (red) under chopped illumination in a pH 5 electrolyte. c, Incident photon to current efficiency and integrated photocurrent density. d, Proposed mechanism for better hole extraction due to the suppression of electron–hole recombination in the CuO/NiO layer.

3.1.5 Elucidating the degradation mechanism of Cu_2O photoelectrodes

To illustrate the stability of Cu_2O photoelectrodes in different pH aqueous solutions, we carried out the soaking test of Cu_2O photocathodes in strong acid (pH 0, 0.1 M H_2SO_4), neutral (pH 5, 0.5 M Na_2SO_4+0.1 M KH_2PO_4) and strong alkaline (pH 14, 1M KOH) solution conditions for several hours, and the results are listed in Figure 6. In pH 5 electrolyte, there was nearly no morphological changes and RuO_x catalysts were still well covering Cu_2O NW photocathodes. This supports our previous results that Cu_2O NW photocathodes are stable in the near-neutral aqueous solution. However, Cu_2O NW structures were damaged and peeled off from the substrates after immersed in the pH 0 aqueous solution. We suspect that the concentrated protons in the strong acid attack and dissolute TiO_2 overlayer. In the following, it accelerates the dissolution of the whole structures of Cu_2O NW photocathodes. In contrast, no apparent damages were visible by naked eyes after soaking test in the pH 14 aqueous solution. The only thing we could observe was that the sample color became slightly darker than the Cu_2O NW photocathode in the pH 5 aqueous solution. Surprisingly, the morphology of Cu_2O NW photocathode was fully changed from smooth surfaces to wrinkled structures after soaking into the pH 14 aqueous solution. It was mainly caused by the change of TiO_2 protection layer because other components including Cu_2O NW and AZO overlayers were not changed at all.

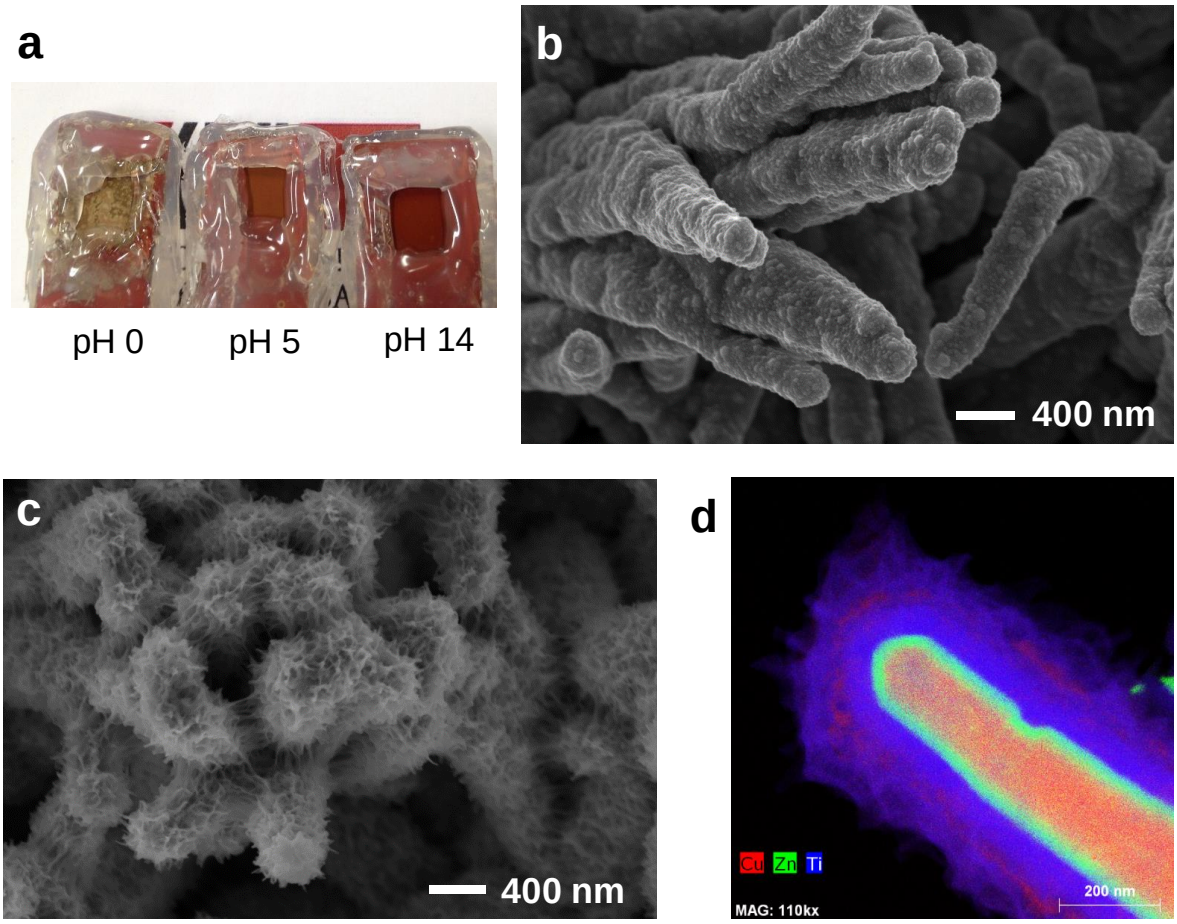

Figure 6: a, Cu_2O NW photocathodes with AZO/TiO_2 overlayers and RuOx catalyst after soaking test for 20 hrs in aqueous solutions with different pH. b, SEM image of Cu2O NW photocathodes after soaking test for 20 hrs in the pH 5 electrolyte. c, SEM image and d TEM image of Cu_2O NW photocathodes after soaking test for 20 hrs in the pH 14 electrolyte.

The thin TiO_2 protection layer expanded to the wrinkled structure, blocking the reactions between the RuO_x catalysts and aqueous solution. Thus, the PEC performance of Cu_2O NW photocathodes becomes unstable in the strong alkaline solution (pH 14) despite there are no peel-offs or huge physical damages.

Although the extreme pH aqueous solutions are necessary for better PEC performances of Cu_2O NW photocathodes, it leads to the poor stability of Cu_2O NW photocathodes due to its morphological changes or physical damages. This means that the TiO_2 protection layer is still not sufficient for protecting Cu_2O NW photocathodes in the extreme pH conditions. In addition, we have explored the crystalline TiO_2 layer for better stability of Cu_2O nanowire photocathodes because it would be more stable in acid or alkaline solutions. Cu_2O nanowire photocathodes were annealed at different temperatures under Ar gas flows to crystallize TiO_2 layer after depositing overlayers. As a result, amorphous TiO_2 layer was successfully converted to crystalline TiO_2 layer above 350 °C. Unfortunately, the Cu_2O nanowire photocathodes largely lost their photoactivity after annealing at such high temperature above 350 °C (Figure 7a), apparently because the Cu_2O nanowire undergoes morphological shrinkage resulting from the high temperature (Figure 7b). Hence, we concluded that this strategy was not suitable for the highly efficient and durable Cu_2O photocathodes.

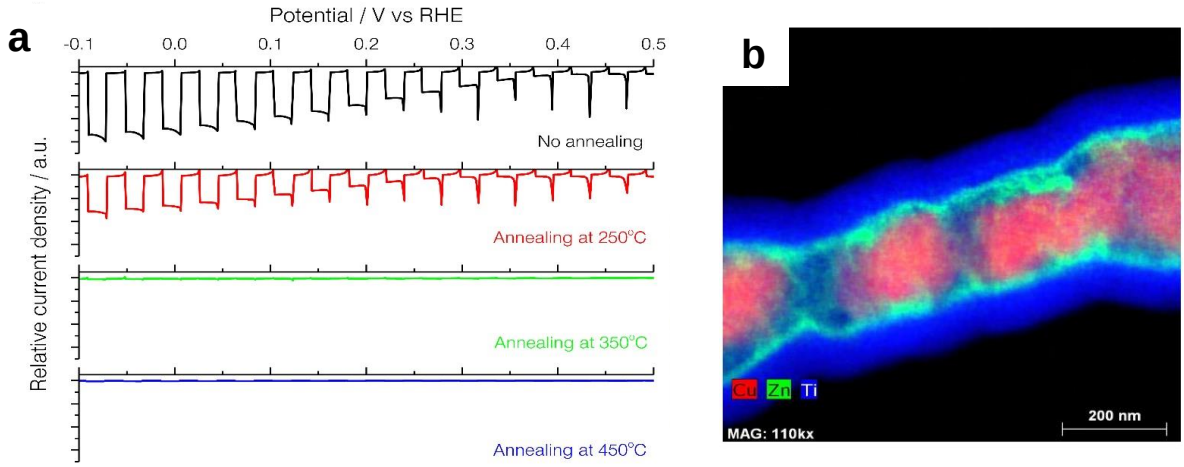

Figure 7: a, Relative PEC performance of AZO-based Cu2O nanowire photocathodes with annealing process at different temperatures under Ar gas flows after depositing overlayers in pH 5 electrolyte. b, TEM images of AZO-based Cu2O nanowire phtocathode with TiO2 overlayers after annealing at 450 °C under Ar gas flow.

Continued works will focus on the crystallization of TiO_2 overlayer without damaging Cu_2O photocathodes, as well as the exploration of alternative protective overlayers, to improve the stability of Cu_2O photocathodes in extreme pH conditions.

3.2 Cu_2S photocathode

With the merits of p-type conductivity, proper bandgap, low toxicity, and high absorption coefficient (>10^4 cm^{-1}), Cu_2S is regarded as a promising material for solar energy conversion. Indeed, it has been widely studied for photovoltaics (PV) since 1960s. With a direct bandgap of 1.8 eV and an indirect bandgap of 1.2 eV, it can theoretically deliver a power conversion efficiency of 30% as a single junction PV cell. Historically, Cu_2S/CdS heterojunction PV devices approached a solar to electricity conversion efficiency of 10%. There are many distinct crystalline phases and stoichiometry of copper sulfide, such as chalcocite (Cu_2S), djurleite ($Cu_{1.96}S$), digenite ($Cu_{1.8}S$), anilite ($Cu_{1.75}S$) and covellite (CuS). However, only Cu_2S can generate free carriers at temperature below 90 °C, as the excess copper deficiency in other compounds will lead to very high hole concentrations, resulting in a degenerately doped semiconductor unsuitable for conventional PV. Therefore, controlling the stoichiometry to achieve the accurate Cu_2S phase is highly important for solar energy application.

There are many methods to prepare Cu_2S films, such as spray pyrolysis, atomic layer deposition (ALD), pulsed chemical vapor deposition (PCVD), electrodeposition, and solid state reaction. However, most of these films are not photoactive because of the poor control of stoichiometry. We use an indirect solution process via ion exchange reaction to prepare Cu_2S from CdS films. The Cu_2S obtained from Cu^+ exchange of CdS is fully stoichiometric, known as the low-chalcocite phase, which is often used in normal structure CdS/Cu_2S solar cells, where CdS is the bottom layer. The Cu_2S phase was confirmed by X-ray diffraction (XRD), Figure 8a. Furthermore, as a photocathode for water splitting, the Cu_2S electrode should be inverted in structure, with the CdS layer on top of the Cu_2S layer. To avoid the oxidation and phase change of Cu_2S during the deposition process of CdS, we

developed a modified chemical bath deposition (CBD) method by adding a reductive agent in the CdS precursor solution. This method results in high quality Cu_2S and CdS p-n junction.

To achieve stable and efficient solar water splitting with Cu_2S/CdS photocathodes, we deposited TiO_2 on the electrode surface as the protection layer and RuO_x as the hydrogen evolution catalyst, Figure 8b. The resulting Cu_2S photocathodes exhibited a photocurrent density up to 7.0 mA cm^{-2} at -0.3 V versus reversible hydrogen electrode (RHE) and an onset potential of 0.48 V vs RHE under AM 1.5G simulated sunlight illumination for photoelectrochemical water reduction, Figure 8c. This performance is comparable to the commonly studied Cu_2O photocathodes. Nevertheless, its smaller bandgap makes it more appealing than Cu_2O to be used as a bottom photoabsorber for tandem solar water splitting devices. Incident photon to current efficiency (IPCE) measurement was carried out at 0 V versus RHE to show the wavelength dependent photoresponse of the electrode, Figure 8d. In agreement with the absorption spectrum of the Cu_2S, the electrode showed a broad response from the ultraviolet to the near-infrared range with a peak efficiency of 51% at 400 nm, confirming the excellent light-harvesting capability. Integrating the IPCE over the standard AM 1.5G spectrum generated a photocurrent density of around 5.5 mA cm^{-2}, consistent with the value obtained from chopped light current–voltage measurement.

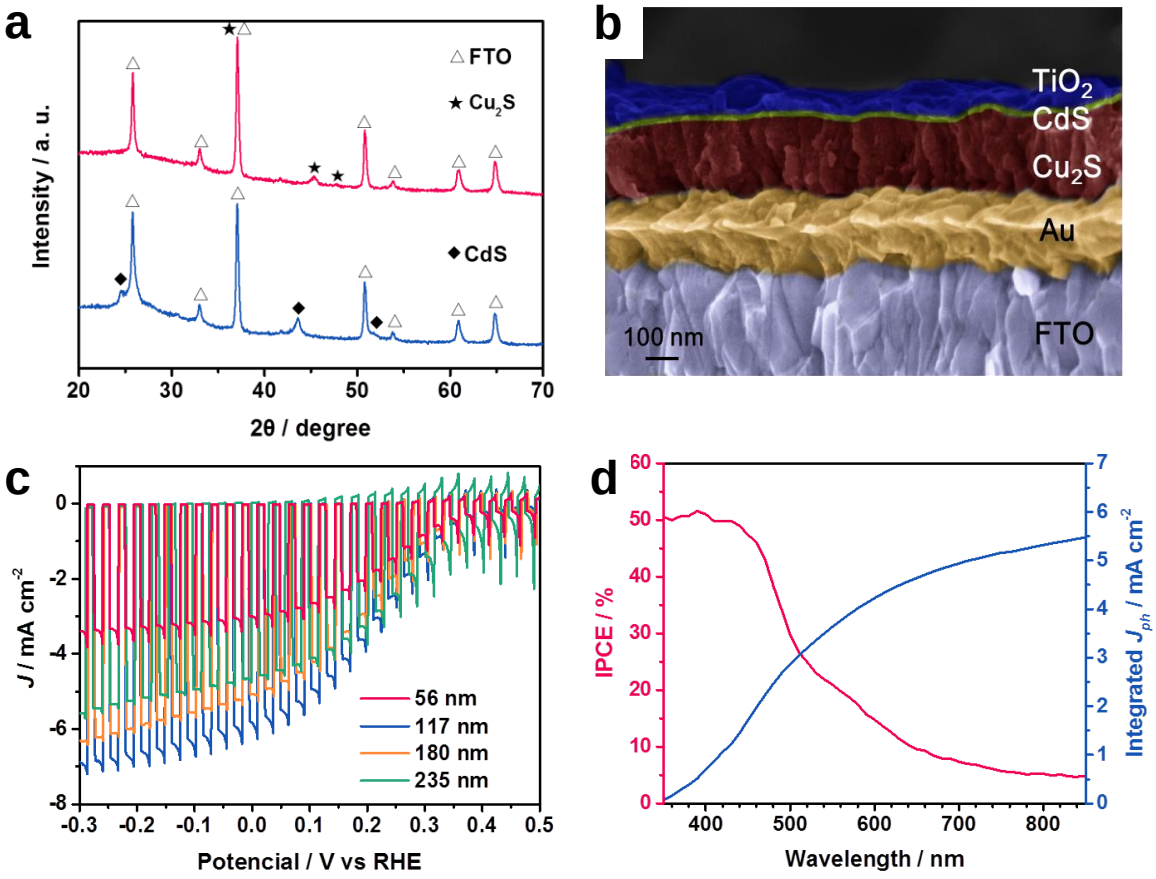

Figure 8: Cu_2S photocathodes. a, X-ray diffraction patterns of prepared films on FTO substrates before (blue) and after (red) ion exchange reaction. b, Cross section false-colored SEM image of the optimized Cu_2S photocathode (FTO/Au/Cu_2S/CdS/TiO_2) with the Cu_2S layer thickness of ca.120 nm. c, J−E curves of Cu_2S photocathodes with different thickness under simulated chopped AM 1.5G illumination. d, IPCE spectra under monochromatic illumination of the optimized Cu_2S photocathode at an applied bias of 0 V vs RHE.

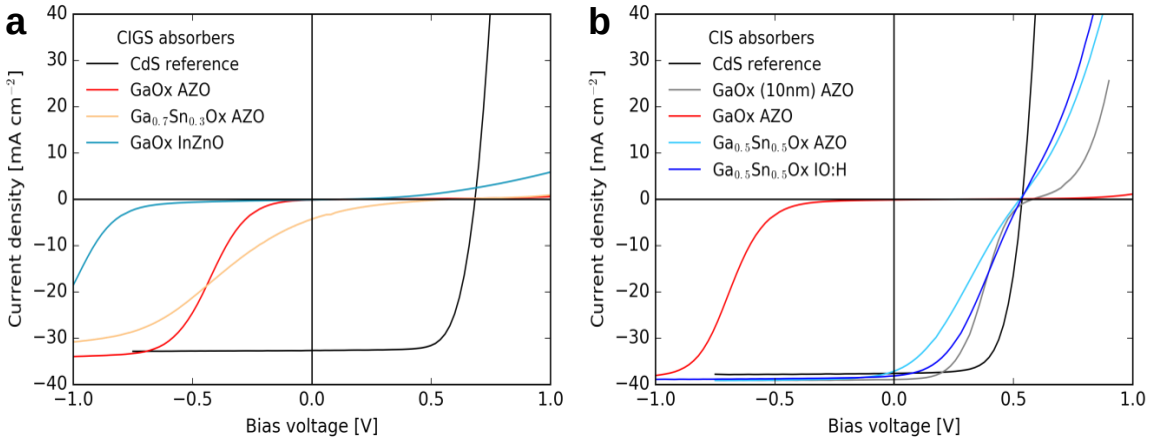

Figure 9: a, Current-voltage curves for a selection of samples with CIGS absorbers, showing a large blocking behavior. The buffer thickness is 30 nm. b, Curves for a selection of samples with low bandgap CIS absorbers. A reduced GaO_x thickness, or a $Ga_{0.5}Sn_{0.5}O_x$ buffer layer composition appear to mitigate the loss in cell efficiency.

To our knowledge, this is the first time that solution processed Cu_2S film has demonstrated appreciable performance for solar water splitting, which will stimulate more studies on Cu-based photocathodes in the future. Because of its small bandgap, it is an appealing bottom photoelectrode for tandem solar water splitting devices. To further increase the photocurrent density, nanostructured electrodes will be used in the future to ensure sufficient light harvesting and provide a short electron transport pathway at the same time. New buffer layers with appropriate band alignment to Cu_2S should be studied to replace the toxic CdS.

3.3 Alternative buffer layer for CIGS solar cells

The most common front contact structure of a CIGS solar cell consists CdS, non-intentionally doped ZnO and Al:ZnO (AZO) layers deposited on top of the CIGS absorber layer. However the 2.4 eV bandgap CdS layer absorbs a significant amount of light, visible in the blue region of the optical spectrum of the external quantum efficiency. As a high bandgap Ga_2O_3 is a possible replacement for CdS. This material deposited by sputtering was notably explored in Ref. [T. Koida et al., IEEE JOURNAL OF PHOTOVOLTAICS, VOL. 5, NO. 3, MAY 2015] together with its alloys with In_2O_3 and Al_2O_3, reaching efficiencies barely lower than the CdS reference. In this project we explored the suitability of GaO_x and $GaSnO_x$ alloys by ALD technique, offering a very conformal coverage of deep recesses of the CIGS surface.

The initial tests conducted in the previous report period appeared relatively successful as the sample exhibited the expected improved spectral response, although the device V_{oc} and FF slightly decreased. In this report period further tests were conducted in view of optimizing the thickness and composition of the buffer layer, and the device ageing stability was studied.

The first samples series explored the influence of the thickness of GaO_x buffer layers on the cells electrical properties, when completed with AZO or ZnO/AZO layers. The best results were obtained with the thickest (30 nm) layers, so thickness was further investigated. Alternative TCO and second buffer layers were also probed (InO:H, InZnO, ZnMgO/AZO). The blocking behavior of the first series suggested unsuitable band alignment at the front interface. Various $GaSnO_x$ alloys were explored, taking advantage of the availability of Sn precursor in the ALD reactor. Finally, low bandgap CIS absorbers were also tested, for which CdS provides a non-ideal band alignment at the front contact.

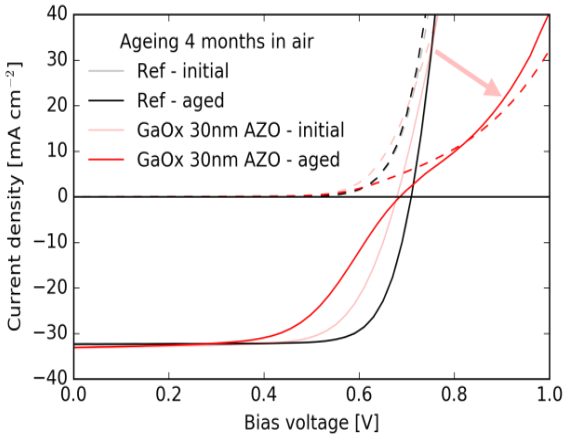

Figure 10: Comparison of current-voltage curves upon 4 months ageing in ambient conditions, for the CdS/ZnO/AZO reference and the GaO_x (30nm)/AZO sample. A blocking behavior becomes pronounced for the sample with GaO_x buffer layer.

Unfortunately, all investigated CIGS samples presented a large blocking behavior as visible in Figure 9a: bias voltages such as -0.5 to -1.2 V were required to extract the photocurrent, including for the sample nominally identical to the best one of the first series. The origin of this large blocking is yet unresolved, as is the cause of the difference with the first sample. The sample exchange is likely not the cause, as a bare reference absorber experienced travelling together with the other samples and proved nearly as good as a reference processed immediately after growth. All ALD parameters were nominally identical and no failure could be evidenced upon a careful check of the different processing steps.

Only the low bandgap CIS samples with $Ga_{0.5}Sn_{0.5}Ox$ or GaO_x 10nm buffer layers did exhibit a lesser degree of blocking, while still significantly worse than the reference, as shown in Figure 9b.

In Figure 10 we compared the current-voltage curves of the reference and of best samples of the first series before and after 4 months ageing under ambient conditions. The blocking behavior is found to worsen. By contrast the CdS reference sample appears stable during the investigated period. The other samples also underwent a degradation marked by an increase in the blocking behavior, independently of the presence of the ZnO second buffer layer. It can be speculated that the GaO_x layer is not stable, and may be subject to changes in composition or doping due to in- or out-diffusion of Ga, In and Al or other species from or to the absorber or window layers.

4 Measurement and modeling of optical and physical processes (WP2)

4.1 Hematite Fe_2O_3

4.1.1 Electrical loss analysis

The interpretation and description of charge transfer processes in metal oxide photoelectrodes still poses considerable challenges in the literature, including intensive discussion about water oxidation from valence band [6] or surface states [3, 2]. Therefore, we implemented surface recombination and trap assisted recombination for Fe_2O_3 in our electrical model developed in PECHouse2 project.

The charge transport in the semiconductor is described by drift-diffusion equations. Note that although SRH recombination is included in the continuity equations, we neglect charge in traps in Poisson's equation. Bulk trap density does not appear in the model parameters in this case. Trap mediated bulk SRH recombination is assumed in hematite

$$R_{SRH} = \frac{np - n_i^2}{\tau_{e,SRH}(p + p_1) + \tau_{h,SRH}(n + n_1)}$$

$$n_1 = n_i e^{\frac{\Delta E_t}{kT}}$$

$$p_1 = n_i e^{\frac{-\Delta E_t}{kT}}$$

where n_i is the intrinsic carrier concentration, $\tau_{e,SRH}$ is the electron SRH lifetime and distance of trap energy level to intrinsic energy level is denoted $\Delta E_t = E_t - E_i$. The steady-state trap occupancy at level E_t is given by relation.

$$f_t = \frac{n_1/\tau_{e,SRH} + p_1/\tau_{h,SRH}}{(n + n_1)/\tau_{e,SRH} + (p + p_1)/\tau_{h,SRH}}$$

which is obtained from a kinetic balance of trapped/emitted electrons and holes. We assume that charge transfer under illumination occurs exclusively from the valence band to the electrolyte. We do not include charge transfer from surface states in the current analysis. The transfer current density of valence band holes at the semiconductor-electrolyte interface (SEI) is described by a first-order approximation

$$j_h(0) = -qk_{trh}\big(p(0) - p_{dark}(0)\big) + j_{BER}$$

where k_{trh} is the rate constant for electron and hole transfer, and a linear dependence on the deviation of the interfacial hole concentration $p(0)$ from its dark value $p_{dark}(0)$ at the interface is assumed. The last term j_{BER} denotes the recombination current due to back electron-hole recombination on the SCLJ, discussed later on. We assume only minority carriers, holes in n-type hematite considered here, are transferred to the electrolyte and no electron transfer from the CB is present.

The physical unit of the rate constant for charge transfer of holes k_{trh} (m/s) is not directly comparable with the rate constant for water oxidation k_{WO} (1/s) as reported in the spectroscopic literature on hematite. The rate constant for water oxidation $k_{WO}$is defined through the number of holes at the surface contributing to the water oxidation photoanodic current

$$j_{WO} = j_e(0) + j_h(0) - j_{BER} = -qk_{trh}\big(p(0) - p_{dark}(0)\big) = -qk_{WO}p_{surf}$$

The recombination current j_{BER} is subtracted from the total current since these charges are lost by recombination and don't contribute to the external circuit.

Typically, holes being able to oxidize water must be close to the SCLJ and the corresponding reaction depth of the semiconductor on the SCLJ is $\delta = 1$ nm. Hence, the volumetric hole concentration at the SCLJ $p(0)$ can be converted to a surface hole concentration by $p_{surf} = \delta p(0)$. The hole current from the equations above describe the same hole oxidation current with different variables, hence we get a relation of the rate constants

$$k_{WO} = k_{trh}/\delta$$

Symbol	Fe_2O_3	Description
N_D [cm^{-3}]	$2.5 \cdot 10^{20}$	Donor concentration
$V_{fb,RHE}$ [V]	+0.4	Flatband potential
χ [eV]	+4.78	Electron affinity
N_C [cm^{-3}	$4 \cdot 10^{22}$	Density of states of CB
N_V [cm^{-3}]	$1 \cdot 10^{22}$	Density of states of VB
ε_r	32	Relative permitivity
E_g [eV]	2.1	Bandgap energy
d [nm]	12	Thickness of semiconductor
μ_e [$cm^2V^{-1}s^{-1}$]	0.016 [a]	Electron mobility
μ_h [$cm^2V^{-1}s^{-1}$]	0.016 [a]	Hole mobility
τ_h [ps]	48	SRH recombination lifetime

[a]order of magnitude value according to Ref. Engel et al. (2014)

Tabelle 1: Material parameters of hematite used in IV and IPCE calculations.

The back electron-hole recombination (BER) [4], also called back-electron transfer in another report, is a surface recombination mechanism. The surface recombination rate constant k_{BER} (unit 1/s) depends on the electron concentration at the surface through the relation

$$j_{BER} = -qk_{BER}p_{surf}$$

$$k_{BER} = v_{th}\sigma_n n(0)$$

where v_{th} is thermal velocity of electrons and σ_n is cross-section for capture of electrons. Hence, the dependency of k_{BER} on potential is contained in $n(0)$. Material parameters entering the model are known with various degree of accuracy, cf. Table 1. The dominant trap energy level for hematite was identified 0.5-0.7 eV below the CB edge (Fe3+ d-d states)[8], here we take $\Delta E_t = 0.5$ eV.

We sought to reproduce measured IV curves on ALD hematite with our calculated IV curves as well as possible. From the parameters entering the model, the 'free' parameter of interest which we're aiming to extract by comparing experimental and simulated results is the rate constant for transfer of holes k_{trh} (rate of water oxidation). Observing that photocurrent onset potential decreases with increasing k_{trh}, we found that rate constant $k_{trh} = 10^{-8}$ m/s best reproduced the measured photocurrent onset

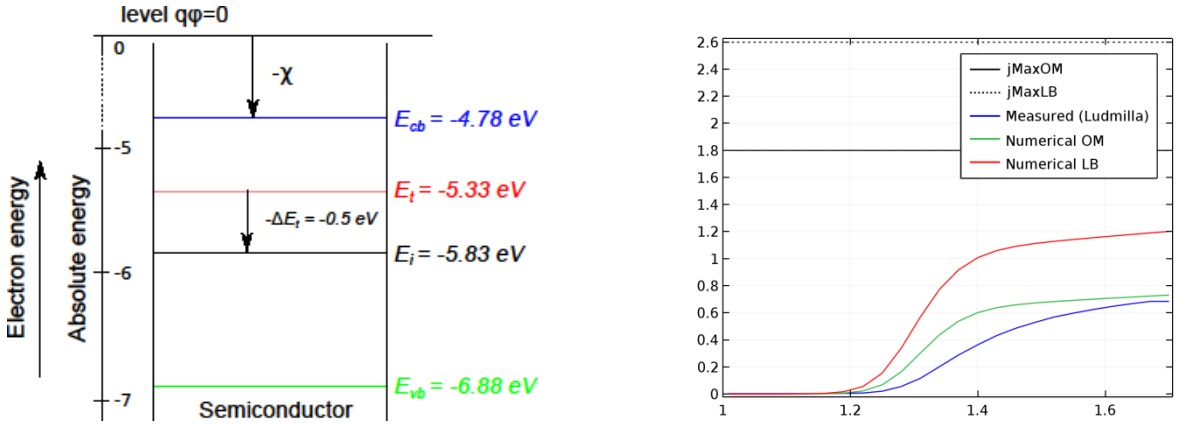

Figure 11: (Left) Sketch of the energy levels of isolated hematite with one discrete trap level at $\Delta E_t = 0.5$ eV. (Right) Comparison of measured (EPFL) and simulated (ZHAW) current-voltage response for EE (front) AM15G illumination, $k_{trh} = 10^{-8}$ m/s.

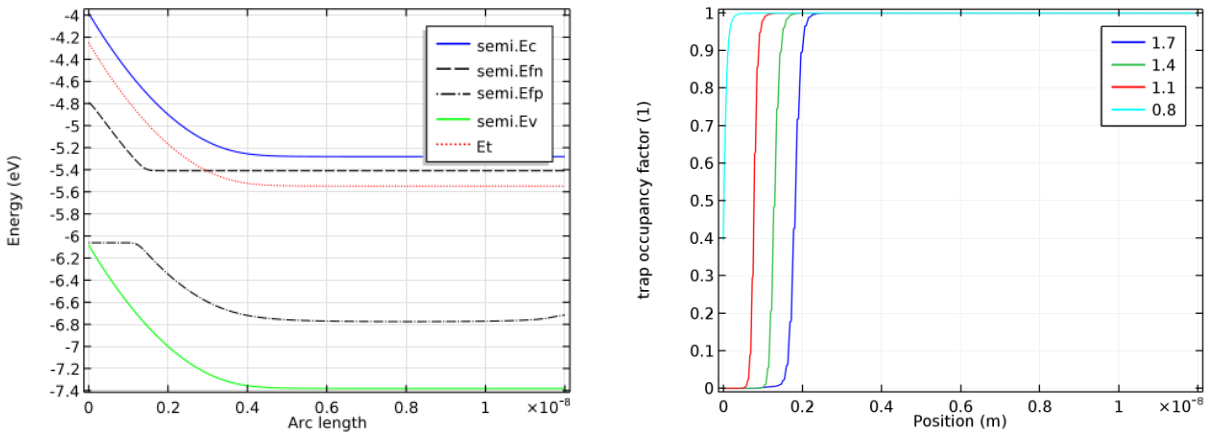

Figure 12: (Left) Calculated energy levels in hematite with one discrete trap level at $\Delta E_t = 0.5$ eV. (Right) Trap occupation for increasing applied voltage.

potential ≈ 1.2 V vs. RHE, Figure 11. Comparison of measured (EPFL) and simulated (ZHAW) current-voltage response for EE (front) AM15G illumination, $k_{trh} = 10^{-8}$ m/s. The calculated IV with generation rate from LB overestimates the electrical current approximately by a factor of 2, while the IV calculated by OM generation rate better approximates the measured IV characteristics, although perfect agreement in IV shape could not be achieved only by varying k_{trh}. The plateau photocurrent ≈ 0.7 mA/cm^2 at 1.7 V vs. RHE agrees well between calculated (OM) and measured data. For comparison, we also show the maximum achievable currents that are obtained when assuming that all absorbed photons contribute (APCE=1) to water oxidation $j_{max,OM}$ (generation rate from optical model) and $j_{max,LB}$ (generation rate from Lambert-Beer LB law). Upon conversion of the rate constant $k_{trh} = 10^{-8}$ m/s to the traditional unit 1/s, we obtain $k_{WO} = 10$ 1/s, in reasonable agreement with the values 0.1-10 1/s reported in the literature [5, 9]. The photocurrent plateau at high potentials depends on the recombination rate and hence on the hole lifetime τ_{SRH} .

Further insights into trap the occupation dynamics are provided by plotting the trap occupation factor in the the semiconductor bulk as shown in Figure 12. For small anodic bias, the traps are filled almost within the whole semiconductor bulk (0.8 $V_{r,RHE}$). For larger anodic bias, an increasingly larger region close to the SCLJ is emptied of traps (Figure 12), and SRH recombination considerably decreases close to the SCLJ, Figure 12.

To quantify the reasons for suboptimal electrical performance and differentiate individual electrical losses in hematite, we calculated IV curves for the following scenarios: Figure 13: i) $j_{max,OM}$ (APCE=1), ii) j_1 without any recombination, iii) j_2 with bulk recombination, iv) j_3 with bulk and surface recombination. For i), it is assumed that all absorbed photons are converted into photocurrent without considering any charge separation losses. For ii) only some charges are separated by the electrical field, but no recombination (bulk nor surface) at all is included in the calculation. The area between $j_{max,OM}$ and j_1 can thus be described as photocurrent loss due to charge separation. In the case iii), the bulk recombination term is included in the model and the resulting photocurrent j_2 is obtained. The area between j_2 and j_1 therefore presents the charges lost by bulk recombination. Finally for iv), also the surface recombination term is included in the calculation and the area between j_3 and j_2 gives solely losses by surface recombination. The effect of the surface recombination on the IV response is also shown in Figure 13, indicating how large losses by surface recombination are for various values of the electron capture cross-section σ.

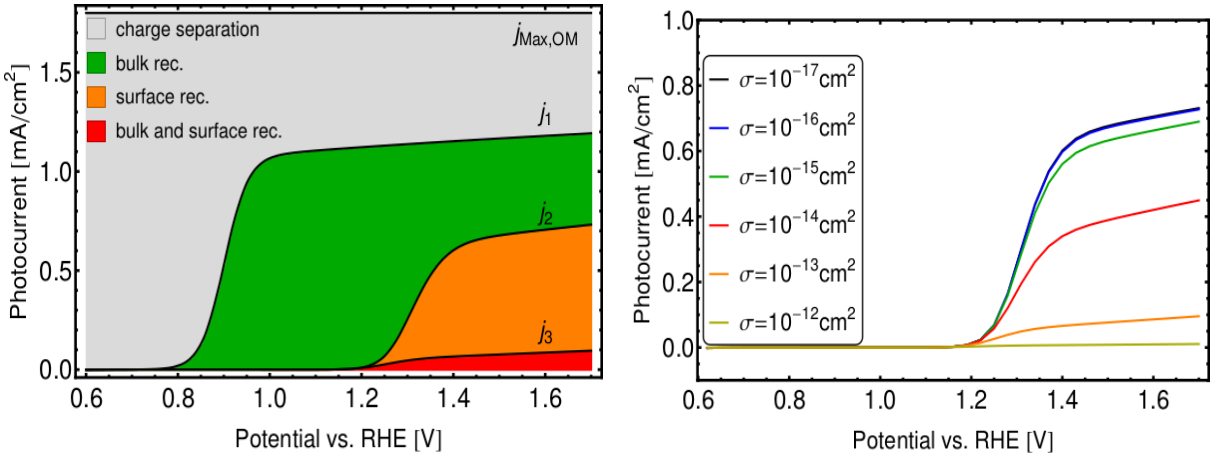

Figure 13: (Left) Calculated electrical losses for parameters: EE (front) AM15G illumination, $\Delta E_t = 0.5$ V, $k_{trh} = 10^{-8}$ m/s, $\tau_{SRH} = 48$ ps, $\sigma = 10^{-13}$ cm^2. (Right) Variation of IV response for different electron capture cross-section σ.

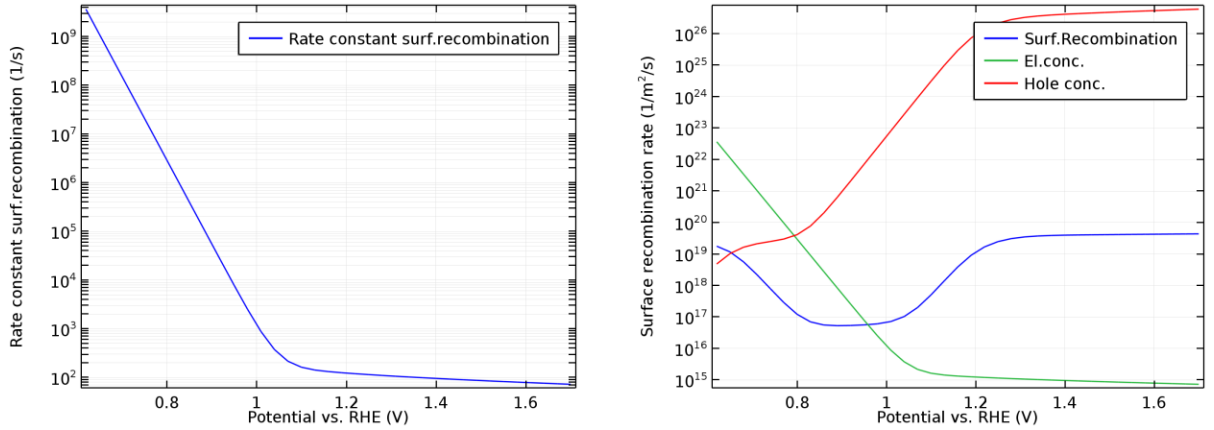

Figure 14: (Left) Surface recombination constant converted to 1/s and (Right) surface recombination rate and carrier concentrations at the SCLJ. Parameters: EE (front) AM15G illumination, $\Delta E_t = 0.5$ V , $k_{trh} = 10^{-8}$ m/s, $\tau_{SRH} = 48$ ps, $\sigma = 10^{-13}$ cm^2.

The decrease of the time constant k_{BER} with applied bias is shown in Figure 14. Currently only at large bias its plateau is 100 s^{-1}. The qualitative increase in surface hole concentration obtained in Figure 14 is in agreement with the increase reported in the literature [7].

4.1.2 Extraction of parameters from PEIS measurements

The rate of water oxidation at a semiconductor-electrolyte interface (denoted here k_{trh}) is usually a limiting factor for many photoelectrode materials. The quantification of the water oxidation rate is not direct in most of the literature sources, but a similar parameter called charge transfer resistance is extracted from an equivalent circuit (EC) of the electrical impedance spectroscopy (EIS) measurement. Although EIS provides means of probing the photoelectrode properties within a large range of characteristic frequencies, its interpretation is not clear and limited to EC models, where various processes and effects from different cell regions are lumped into quantities ascribed to effective EC elements. Thus, EC models usually provide phenomenological parameters rather than system parameters characteristic to certain physical processes.

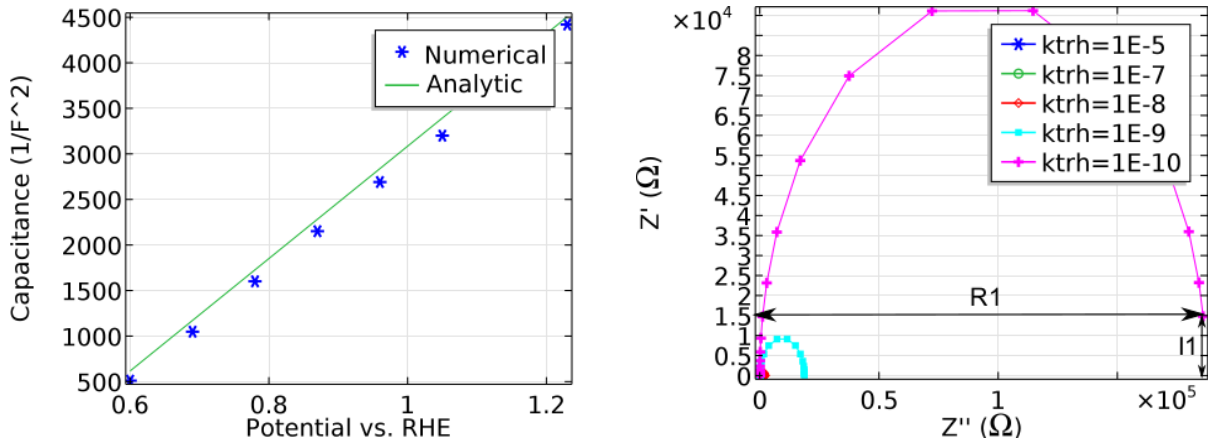

Figure 15: (Left) Mott-Schottky plot of impedance in the dark. (Right) Nyquist plot of impedance under illumination for various values of k_{trh} and fixed potential 0.7 V vs. RHE.

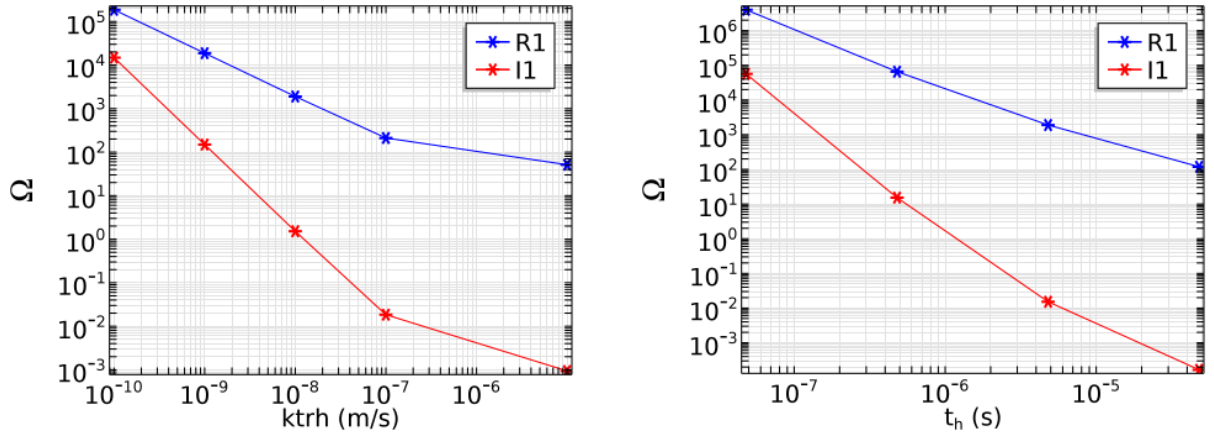

Figure 16: Dependence of lowest frequency (10^{-3} Hz) impedance for 0.7 V vs. RHE on **(left)** rate of water oxidation $\boldsymbol{k_{trh}}$ for fixed $\boldsymbol{t_h = 48 \cdot 10^{-7}}$ s and **(right)** hole recombination lifetime $\boldsymbol{t_h}$ for fixed $\boldsymbol{k_{trh} = 10^{-8}}$ m/s.

To overcome this bottleneck, we have derived a transient drift-diffusion model [1] of EIS and used it to extract physical parameters by means of numerical device simulation. In EIS the cell is operated at certain operating conditions (illumination, cell potential), and a small harmonic potential perturbation is applied to the PEC cell. To reflect the measurement conditions in our simulations, we numerically solve for a stationary solution first and then we assume that the transient solution can be linearized around the stationary solution. In this way, we arrive at a system of partial differential equations for the perturbed variables and solve them numerically in the frequency domain.

We have used material parameters of a hematite photoanode for our calculations. Without light illumination, impedance spectra at low frequency are used to extract doping level and flatband potential of the photoanode from the comparison with the Mott-Schottky analytic formula, Fig. 5. Under light illumination, transient simulations for a range of frequencies 10^{-3}-10^{7} Hz is undertaken and presented in the form of a Nyquist plot, Figure 5. The Nyquist plots exhibit a single semicircle, pointing to a capacitive behavior of the electrode. We investigated the dependence of the real (R_1) and imaginary (I_1) part of the lowest frequency impedance on the rate constant k_{trh}, for a potential of 0.7 V vs. RHE, slightly higher than the flatband potential, Figure 16.

The linear relation between R_1 and k_{trh} is obtained from simulations, Figure 16. A similar relation was obtained between R_1 and the recombination rate t_h (not shown). Thus, governing processes for the semicircle size are both electron-hole recombination and the rate of water oxidation. Their values can be extracted from a comparison of measured and simulated impedance data.

4.2 Cuprous oxide Cu_2O

Since the first investigations of a Cu_2O photocathode at LPI EPFL during PECHouse project, its 'photovoltage' was one of the limiting factors. Specifically, only until last year the layer configuration was TiO_2/AZO/Cu_2O with 'photovoltage' ~0.3-0.6 V. In this modeling section, we will rather use the term onset potential V_{on} (at which photocurrent reaches 0.1 mA/cm2) instead of 'photovoltage'. Photovoltage for hydrogen evolution is equal to the onset potential since the reaction happens at 0V vs RHE.

Following the developments in Cu_2O photovoltaic devices, the replacement of AZO with Ga_2O_3 has recently improved the measured photovoltage to ~1.1 V at LPI EPFL. In this task we focused on an analysis of the mechanism leading to this photovoltage improvement. We aim to reproduce the current-voltage measurements with numerical simulations and to provide theoretical guidelines for best Cu_2O photocathodes.

Model assumptions:

- no interface recombination
- band edge pinning at electrolyte interface
- TiO_2 conducts electrons as good as metal, hence we omit TiO_2 from semiconductor modelling
- charge transfer from CB of AZO or Ga_2O_3 to the electrolyte (rate constant k_{tre})
- direct recombination
- thermionic emission at internal interfaces

4.3 Comparison of AZO-Cu_2O and Ga_2O_3-Cu_2O behaviour

The mechanism influencing the value of the photocurrent onset potential V_{on} is the formation of an energy barrier for electrons at one of the interfaces or the limited rate of hydrogen evolution (k_{tre}).The height of the energy barrier is influenced mostly by band alignments between individual semiconductors and their bandgaps. With the literature values of electron affinity for AZO (4.4 eV) and Ga_2O_3 (3.2 eV), the simulated values of V_{on} are ~1.1 V vs RHE and ~1.6 V vs RHE, respectively, see Figure 7. On the band diagram plot of a junction with AZO, we observe the energy barriers at the SCLJ and AZO/Cu_2O interfaces for 1.5 V vs RHE, whereas for 0 V vs RHE there are no such energy barriers. For a junction with Ga_2O_3 we observe the energy barrier at the SCLJ beyond 1.7 V vs RHE, hence the onset potential is more positive than with AZO. The rate constant for CB electron transfer from the buffer layer to the electrolyte k_{tre} is assumed to have the same value 10^{-5} m/s for both buffer layers. Decreasing k_{tre} (slowing down hydrogen evolution at the interface) shifts V_{on} to less positive values and eventually one could achieve overlap with measured V_{on} – however, convergence difficulties in the numerical solution preclude us so far to draw conclusions on this point. We note that other physical processes may be responsible for the observed V_{on} as well, such as interface recombination, interfacial states and kinetic effects. Our work deems to use simplest assumptions with a low number of free material parameters to qualitatively reproduce the experimental behaviour. As understanding of the materials and their characterization will become more accurate, refined models of the charge transport in the Cu_2O photocathode can be developed and validated.

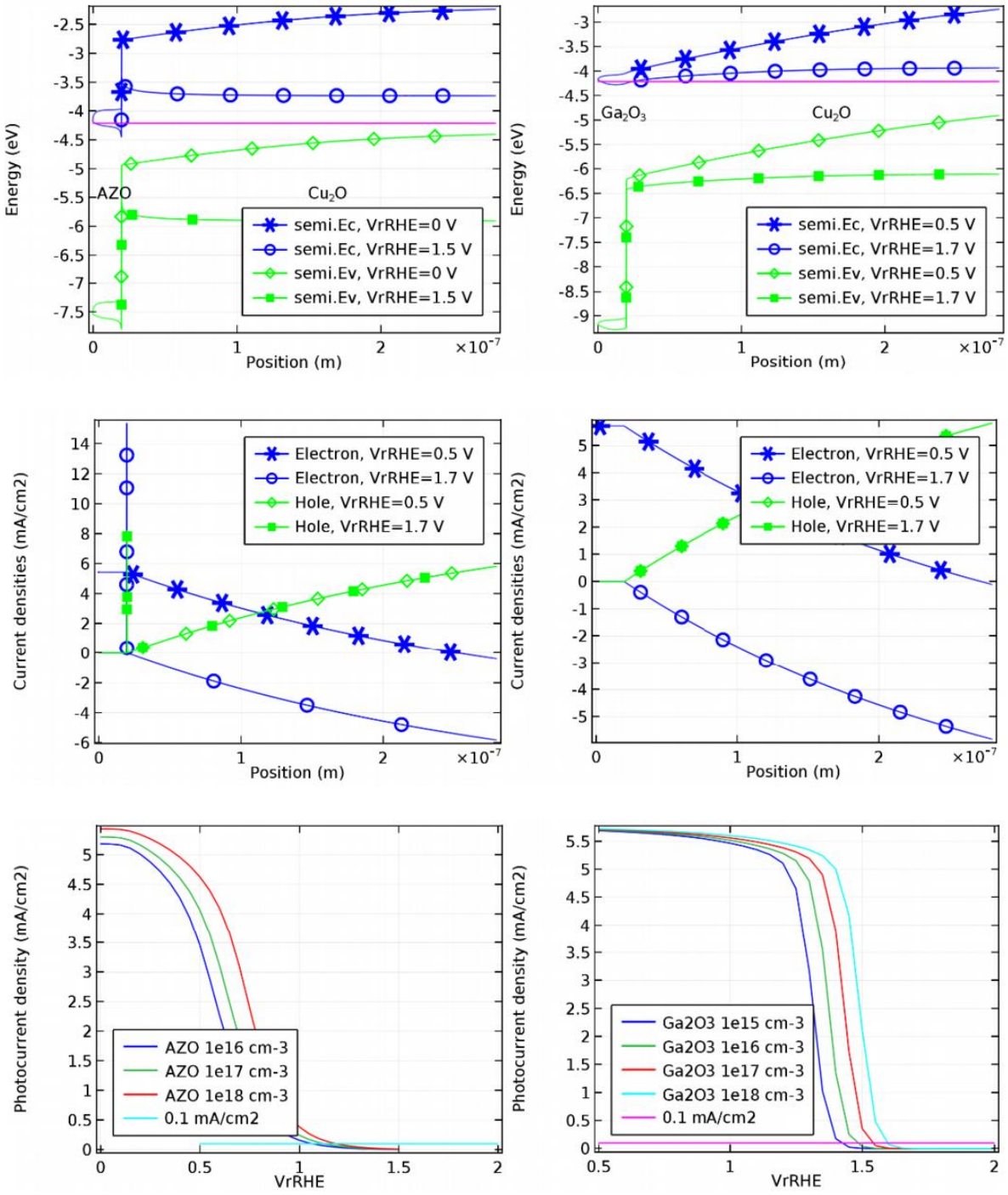

Figure 17: (left column) AZO–Cu_2O and (right column) Ga_2O_3 –Cu_2O junction behaviour. Band diagrams, partial current densities are shown at two representative voltages for buffer doping 10^{18} cm^{-3}. Finally, the current–voltage with varied doping of the buffer layer is shown.

Doping of Ga_2O_3 should increase the built-in potential of the junction since the analytical estimate for the junction in the dark under thermal equilibrium reads

$$V_{bi} = \frac{E_{gp} + \Delta E_c + k_b T \ln(\frac{N_A N_D}{N_C N_V})}{q}$$

$$\Delta E_c = \chi_p - \chi_n$$

$$V_{bi,p} = \frac{N_D}{N_D + N_A} V_{bi}$$

$$V_{bi,n} = \frac{N_A}{N_D + N_A} V_{bi}$$

Hence for larger N_D one obtains larger V_{bi}. For doping values specified by LPI EPFL,the equation gives $V_{bi} = 0.9$ V with AZO doping $2 \cdot 10^{21}$ cm^{-3} and $V_{bi} = 1.8$ V with Ga_2O_3 doping $3 \cdot 10^{16}$ cm^{-3}. These values indicate a trend which is experimentally observed (doubling of photovoltage), however the actual values are shifted since the details of transfer kinetics are not incorporated in the equations above. Similarly, the V_{on} values computed from our drift-diffusion model shows the same trend as observed experimentally, whereas the numerical values of V_{on} are shifted also. Undergoing work at LPI EPFL targets higher doping of Ga_2O_3. Based on the above equations we estimate an improvement of the photovoltage by 0.1-0.2 V by going from doping $3 \cdot 10^{16}$ to $1 \cdot 10^{18}$ cm^{-3}.

4.3.1 Photovoltage dependence on conduction band offset

We studied how engineering the conduction band offset (CBO) from TiO_2 (varying) to Cu_2O (fixed) affects the IV curve of a PEC device. It is of particular interest to study how it influences the onset voltage of the photocurrent (V_{on}, defined as voltage where current passes 0.1 mA/cm^2). This is shown in Figure 18. We observe an increase in V_{on} for smaller CBO between Cu_2O and TiO_2. Hence we infer that also Ga_2O_3/Cu_2O with CBO of nearly 1.2 V will behave similarly to TiO_2/Cu_2O with this artificial CBO and provide larger V_{on} compared to AZO/Cu_2O which has a CBO of nearly 0V. Our model should be understood as one of the simplest qualitative predictions for Cu_2O photocathode HJ, with likely modeling improvements in future when more knowledge is gathered on defect chemistry in HJ.

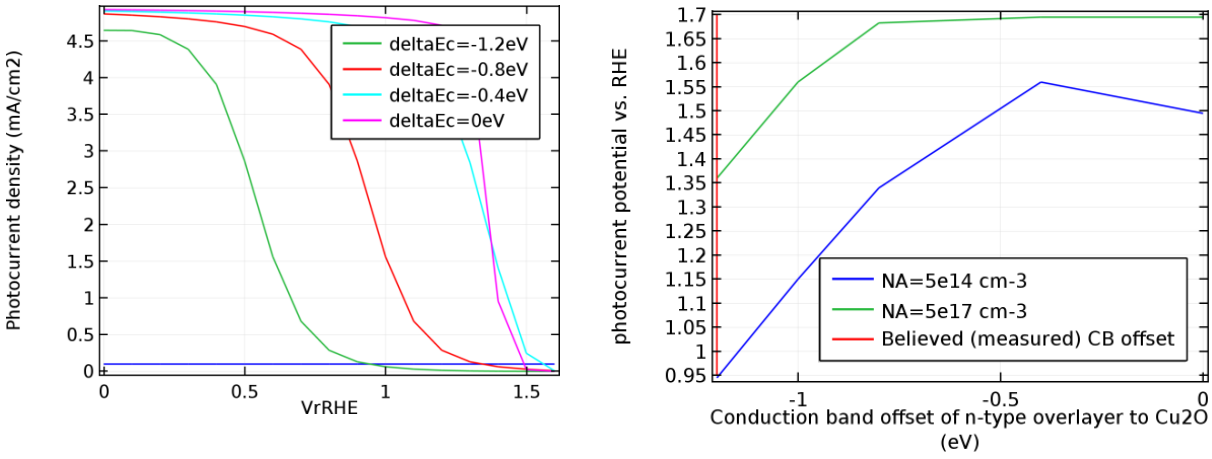

Figure 18: Dependence of lowest frequency (10^{-3} Hz) impedance for 0.7 V vs. RHE on (left) rate of water oxidation k_{trh} for fixed $t_h = 48 \cdot 10^{-7}$ s and (right) hole recombination lifetime t_h for fixed $k_{trh} = 10^{-8}$ m/s.

References

[1] P. Cendula. Final project report h2-nrp70, snsf no. 407040-154002. 2017.

[2] Benjamin Klahr, Sixto Gimenez, Francisco Fabregat-Santiago, Juan Bisquert, and Thomas W. Hamann. Electrochemical and photoelectrochemical investigation of water oxidation with hematite electrodes. *Energy & Environmental Science*, 5(6):7626–7636, May 2012.

[3] Benjamin Klahr, Sixto Gimenez, Francisco Fabregat-Santiago, Thomas Hamann, and Juan Bisquert. Water Oxidation at Hematite Photoelectrodes: The Role of Surface States. *J. Am. Chem. Soc.*, 134(9):4294–4302, 2012.

[4] Florian Le Formal, Stephanie R. Pendlebury, Maurin Cornuz, S. David Tilley, Michael Grätzel, and James R. Durrant. Back Electron–Hole Recombination in Hematite Photoanodes for Water Splitting. *Journal of the American Chemical Society*, 136(6):2564–2574, February 2014.

[5] Stephanie R Pendlebury, Alexander J Cowan, Monica Barroso, Kevin Sivula, Jinhua Ye, Michael Grätzel, David R Klug, Junwang Tang, and James R Durrant. Correlating long-lived photogenerated hole populations with photocurrent densities in hematite water oxidation photoanodes. *Energy Environ. Sci.*, November 2011.

[6] Stephanie R Pendlebury, Xiuli Wang, Florian Le Formal, Maurin Cornuz, Andreas Kafizas, S. David Tilley, Michael Grätzel, and James R Durrant. Ultrafast Charge Carrier Recombination and Trapping in Hematite Photoanodes under Applied Bias. *Journal of the American Chemical Society*, 136(28):9854–9857, July 2014.

[7] Laurence M. Peter. Energetics and kinetics of light-driven oxygen evolution at semiconductor electrodes: the example of hematite. *Journal of Solid State Electrochemistry*, 17(2):315–326, February 2013.

[8] Kevin Sivula. Metal Oxide Photoelectrodes for Solar Fuel Production, Surface Traps, and Catalysis. *The Journal of Physical Chemistry Letters*, 4(10):1624–1633, May 2013.

[9] K.G. Upul Wijayantha, Sina Saremi-Yarahmadi, and Laurence M. Peter. Kinetics of oxygen evolution at α-Fe_2O_3 photoanodes: a study by photoelectrochemical impedance spectroscopy. *Physical Chemistry Chemical Physics*, 13(12):5264, 2011.

5 Water splitting tandem device demonstrations (WP3)

5.1 Bipolar membrane assisted solar water splitting in optimal pH

In an overall water splitting system, catalyst design has to be considered for both reactions. In order to realize efficient and long term water splitting, a strong acid or base electrolyte has to be used to increase the conductivity and minimize the pH gradient that arises from the proton consumption at the cathode and proton production at the anode. Such a requirement limits the choice of available catalysts, as most of the efficient and Earth-abundant oxygen evolution catalysts are not stable in acidic condition, and vice versa; most of the efficient and Earth abundant hydrogen evolution catalysts are not stable in base. Most of the commercially available electrolysers run in either strong acid or strong base electrolyte. In these systems, the highly corrosive environment limits the choice of catalysts, and they suffer from the high cost of finding compatible catalysts for hydrogen evolution and oxygen evolution in one electrolyte. For example only precious metal catalysts made from Ir and Ru can evolve oxygen efficiently in an acidic environment, making acid-based electrolysis a difficult environment. Furthermore, in order to avoid the mixture of H_2 and O_2 gas generated, which not only add additional cost for purification but also might cause an explosion of the system, a membrane is necessary to separate the products. Due to its unique feature in separating the electrolytes and maintaining a significant pH gradient, the bipolar membrane (BPM) has recently caught attention for water splitting applications. The use of a BPM could break the pH incompatibility of the

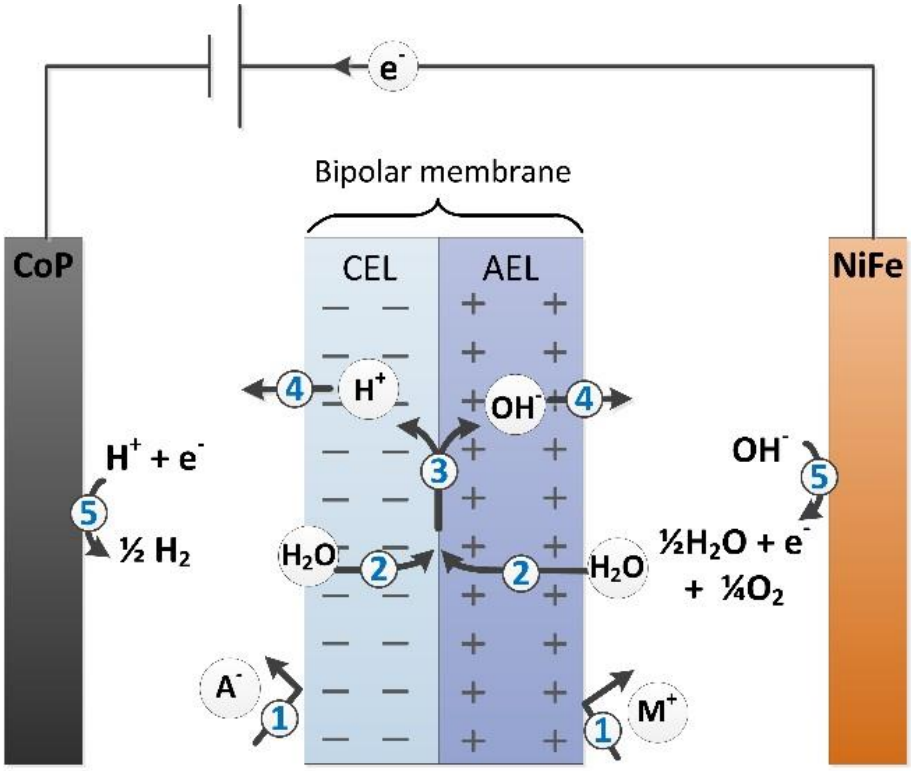

Figure 19: The operating principle and the schematic diagram of the bipolar membrane based water splitting system.

electrocatalysts, opening up a new door towards the water splitting system design by allowing the separate optimization of catalyst/electrolyte pairing of the two half-reactions of water splitting irrespective of the counter electrodes environment. The operating principle and the schematic diagram of the bipolar membrane based water splitting system are depicted in Figure 19. During operation, the bipolar membrane blocks the anion transport from the cathode compartment to the anode compartment through the cation exchange layer and the cation transport from the anode compartment to the cathode compartment through the anion exchange layer, as shown in process **1**. At the same time, water can penetrate both the cation exchange layer and the anion exchange layer of the bipolar membrane, as shown in process **2**. Due to the built in electric field, water starts to dissociate at the interface of the cation exchange layer and anion exchange layer and releases protons (H^+) and hydroxyl ions (OH^-), as shown in process **3**. When an electric field is applied between the anode and cathode, H^+ ions migrate through the cation exchange layer to the cathode compartment, while the migration of the OH^- ions through the anion exchange layer to the anode compartment, as shown in process **4**. H^+ ions are reduced into H_2 on the surface of the cathode and OH^- ions are oxidized into O_2 on the surface of the anode, as shown in process **5**. These five processes operate simultaneously and help to maintain the pH in each compartment. For an ideal bipolar membrane, the balance between H^+ and OH^- consumption in the HER and OER exactly equals the H^+ and OH^- production in the BPM.

In catalysis, transition metal phosphides have surpassed sulfides in performance as efficient hydrogen evolution catalysts for water splitting in acid conditions, demonstrating an earlier onset potential and a higher current density. At the same time, NiFe layered double hydroxide (LDH) remains as one of the best oxygen evolution catalysts in base. Considering both the high activity and the low cost of materials, in this project we choose CoP and NiFe LDH, both made from solution-based synthetic methods, as the catalysts for HER in acid and OER in base, respectively. With a BPM for gas

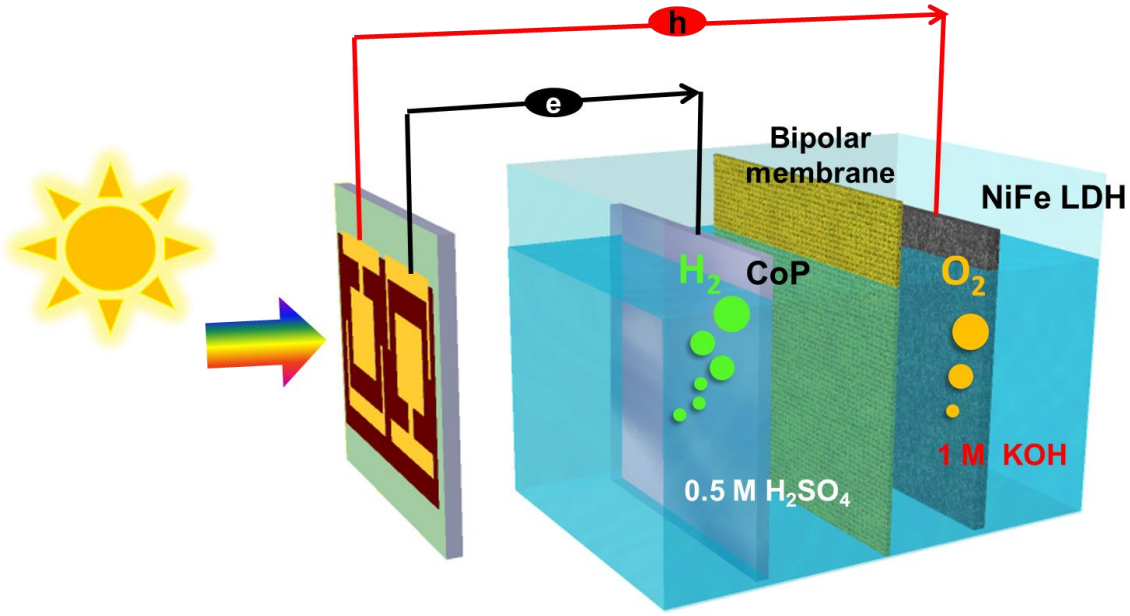

Figure 20: Schematic diagram of the solar driven water splitting device composed of perovskite light harvesters, Earth-abundant catalysts and bi-polar membrane.

separation and maintaining the pH gradient in the two compartments, we built an efficient and intrinsically safe solar-driven water splitting system, composed of the state-of-the-art Earth-abundant catalysts for hydrogen evolution in acid and oxygen evolution in base and perovskite light harvesters. To drive our electrolysis system composed of Earth-abundant materials with solar irradiation, we choose perovskite solar cells as the light harvesting materials. Perovskite solar cells have shown great promise for solar energy conversion due to their high efficiency and facile solution based fabrication process, allowing inexpensive photovoltaics cells to be achieved in a short amount of time. The main advantage of perovskite solar cells for solar fuel generation is their large photovoltage, sufficient to drive efficient overall water splitting by connecting only two cells in series, which is not possible for conventional Si and thin film CIGS solar cells. Following our previous work, we use two perovskite solar cells connected in series and wired to the catalyst electrodes as the driving force, as depicted in Figure 20.

The operating current of the system can be predicted by plotting the *J*-V curves of the tandem perovskite solar cell and the catalyst electrodes together, Figure 21a. The operating current when connecting the tandem perovskite solar cell to the electrolysis cell is measured under chopped light illumination for 16 h, Figure 21b. Overall, the system shows an initial photocurrent density of ~10.35 mA cm^{-2}, corresponding to a STH conversion efficiency of 12.7%. After 16 hours' operation, the system still retains a photocurrent density of ~7.35 mA cm^{-2}, corresponding to a STH conversion efficiency of 9%. This system serves as the model architecture for the future development and optimization of the individual components of an overall water splitting system.

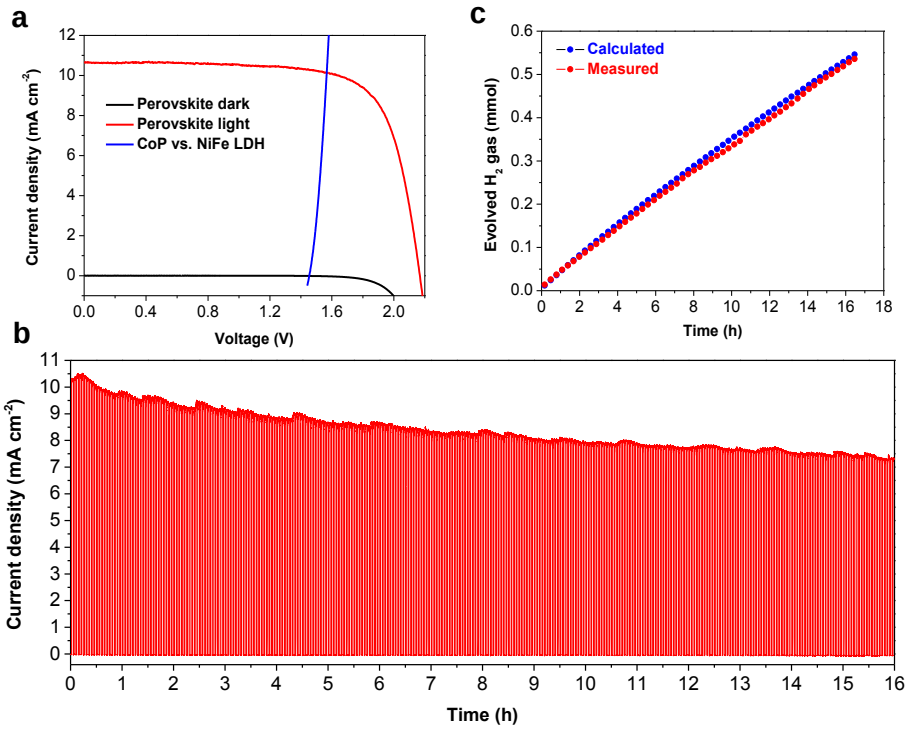

Figure 21: Solar driven water splitting with perovskite light harvesters and bipolar membrane cell. (a) *J*–V curves of the perovskite tandem cell under dark and simulated AM 1.5G 100 mW cm^{-2} illumination, and the catalyst electrodes in bipolar membrane cell. The illuminated surface area of the perovskite cell was 0.32 cm^2, and the catalyst electrode areas (geometric) were 2.27cm^2 each. (b) Stability test of the integrated solar water splitting system without external bias under chopped simulated AM 1.5G 100 mW cm^{-2} illumination. (c) Quantification of the evolved H_2 and O_2 gas during the stability test of the integrated solar water splitting system with GC.

5.2 Cu_2O-$BiVO_4$ photoelectrochemical tandem

For this system, we use Cu_2O as a photocathode and $BiVO_4$ as a photoanode to build an all-oxide based tandem solar water splitting device. At present, these materials are the besting performing photoelectrodes among all metal oxides. Given the efforts carried out in advancing the performance of Cu_2O photocathode and the development of novel protection layers, we have achieved an STH efficiency of 3% for this device, which is a new record for PEC water splitting using only inexpensive and Earth-abundant materials, Figure 22.

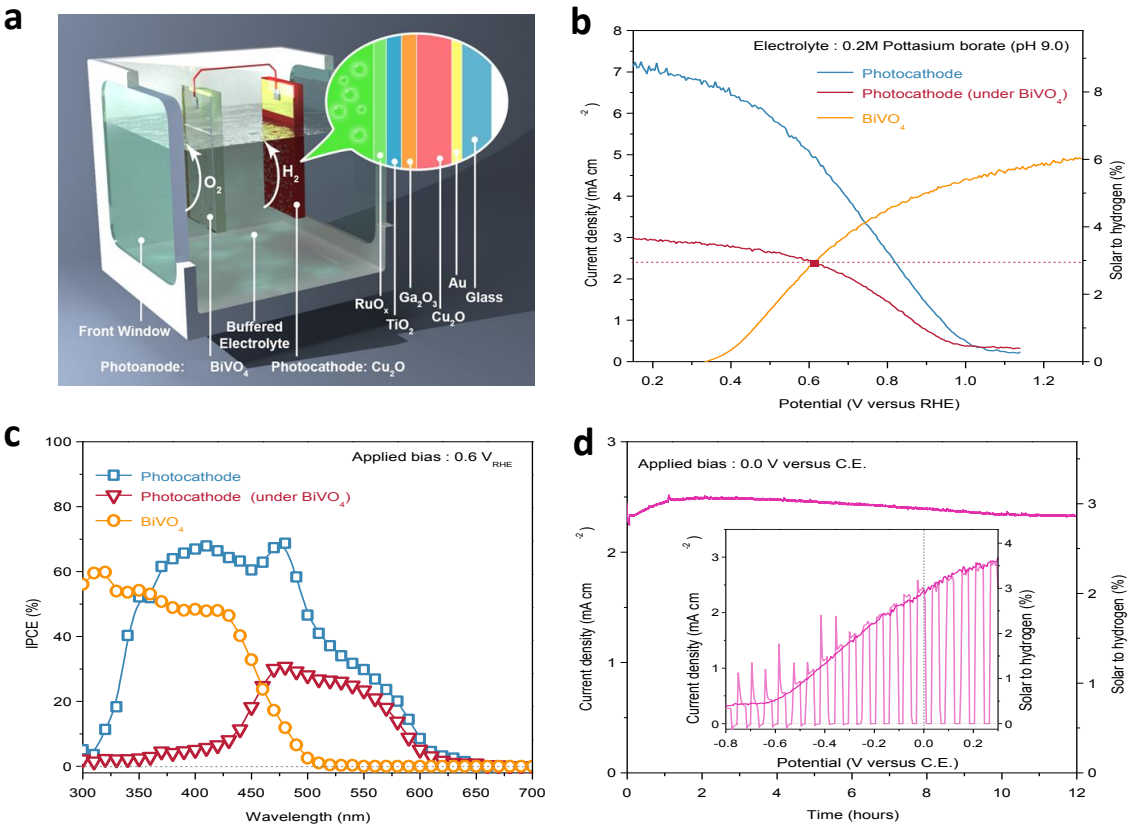

Figure 22: Cu_2O and $BiVO_4$ tandem device for overall solar water splitting. a, Schematic diagram of Cu_2O and $BiVO_4$ tandem. b, *J*-V curves of Cu_2O and $BiVO_4$ photoelectrodes in three electrode configuration. c, IPCE spectra of Cu_2O and $BiVO_4$ photoelectrodes in three electrode configuration. d, Current density and solar to hydrogen conversion efficiency of Cu_2O and $BiVO_4$ tandem in two electrode configuration.

5.3 Scale-up demonstration of Cu_2O photocathode

We began efforts to translate the test-scale device designs to scaled-up dimensions. We established a cell geometry using Cu_2O photoelectrodes with dimensions of 5 x10 = 50 cm^2 which can be arranged in a 4x array to achieve the ultimate goal of 200 cm^2. The 50 cm^2 Cu_2O photocathode prototype has silver contacts on edges for better charge collection over large areas. We scaled up the AZO-based transparent Cu_2O photocathodes (Figure 23 a, b) using the optimal conditions in the test-scale device. We successfully demonstrated the 50 cm^2 devices with homogeneous Cu_2O deposition using Ag grid structure showing photocurrent onsets of 0.55 V vs RHE and photocurrent density of 2 mA/cm^2 at 0 V vs RHE in pH 5 electrolyte under similar intensity of 0.6 sun illumination, Figure 23c.

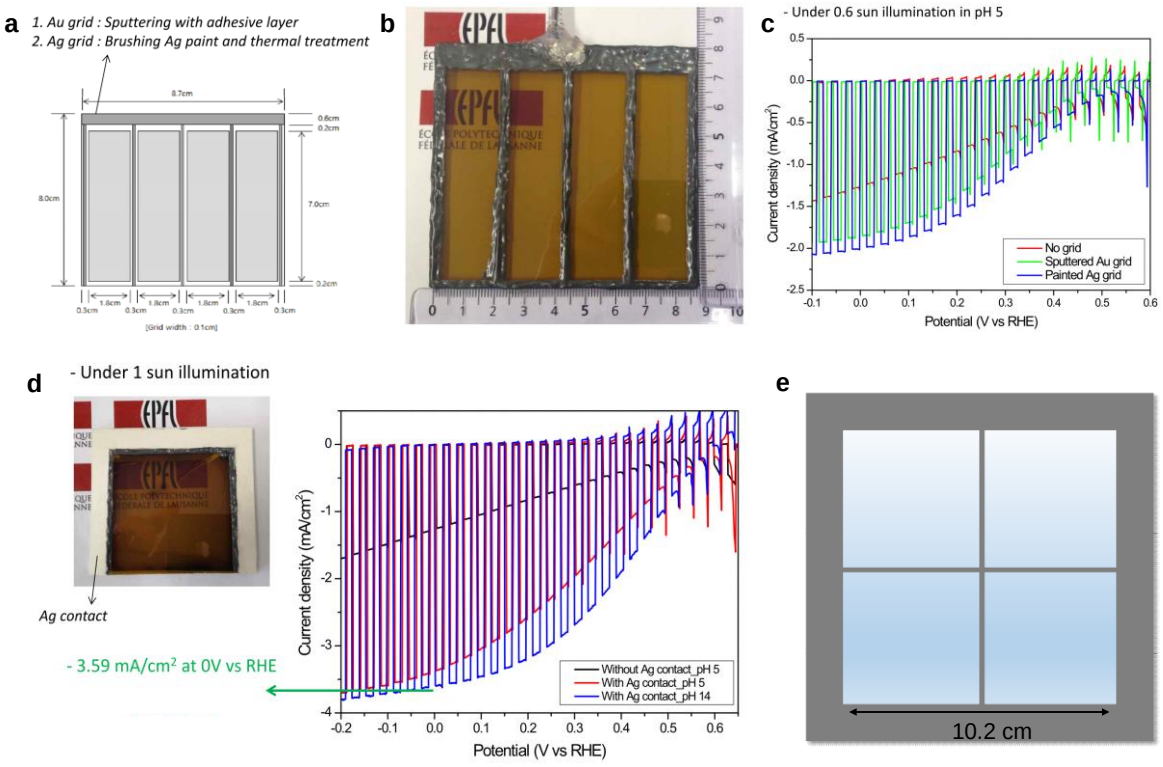

Figure 23: Large-scale Cu_2O photocathodes. a, Design of a Cu_2O photocathode with an active area of 50.4 cm^2 using Ag grid structure. b, Photo of the 50.4 cm^2 Cu_2O photocathode using Ag grid. c, *J*-V curves of Cu_2O photocathodes with various designs. d, Design of a Large scale Cu_2O photocathode with a dimension of 5x5 cm^2. e, Design of a 100 cm^2 large scale electrode using four (5x5 cm^2) mosaic cells.

We also made a different Cu_2O photocathode with a dimension of 5x5 cm^2, Figure 23c. This electrode shows a photocurrent of 3.8 mA cm^2 under one sun illumination condition and an onset potential of ~0.6 V. Using four such mosaic cells, we can build a large-scale Cu_2O photoelectrode with a size of 100 cm^2. The demonstration of 50 cm^2 and 25 cm^2 Cu_2O photocathodes forms the basis of successful scale-up demonstration of optimal tandem around 200 cm^2 for PECHouse3 project. Future works will focus on more efficient and stable large-scale Ga_2O_3-based Cu_2O photocathodes by optimizing the metal grid lines and introducing large-scale Cu_2O nanowire photocathodes.

6 PECHouse3 publications to date:

[1] P. Cendula, L. Steier, P. A. L, M. Grätzel, J. O. Schumacher, Analysis of Optical Losses in a Photoelectrochemical Cell: A Tool for Precise Absorptance Estimation, Adv. Funct. Mater. 2017, 1702768, DOI: 10.1002/adfm.201702768.

[2] M.-K. Son, L. Steier, M. Schreier, M.T. Mayer, J. Luo, M. Grätzel, Copper Nickel Mixed Oxide Hole Selective Layer for Au-Free Transparent Cuprous Oxide Photocathodes, Energy Environ. Sci. (2017), 10, 912-918. doi:10.1039/c6ee03613a.

[3] C. Mesa, A. Kafizas, L. Francas, S. R. Pendlebury, E. Pastor, Y. Ma, F. Le Formal, M.T. Mayer, M. Grätzel, J.R. Durrant, Kinetics of Photoelectrochemical Oxidation of Methanol on Hematite and Anatase Photoanodes, J. Am. Chem. Soc., (2017), 139,11537–11543. DOI: 10.1021/jacs.7b05184.

[4] L.-A. Stern, L. Liardet, M.T. Mayer, C.G. Morales-Guio, M. Grätzel, X. Hu, Photoelectrochemical deposition of CoP on cuprous oxide photocathodes for solar hydrogen production, Electrochim. Acta. (2017), 235, 311-316, doi: 10.1016/j.electacta.2017.03.074.

[5] E. Pastor, F. Le Formal, M.T. Mayer, S.D. Tilley, L. Francas, C.A. Mesa, M. Grätzel, J.R. Durrant, Spectroelectrochemical analysis of the mechanism of (photo)electrochemical hydrogen evolution at a catalytic interface, Nat. Commun. (2017), 8, 14280, doi:10.1038/ncomms14280.

[6] M.T.Mayer, Photovoltage at semiconductor–electrolyte junctions, Current Opinion in Electrochemistry, (2017), 1, 104-110, doi:10.1016/j.coelec.2017.03.006.

[7] J. Azevedo, S.D. Tilley, M. Schreier, M. Stefik, C. Sousa, J.P. Araújo, A. Mendes, M. Grätzel, M.T. Mayer, Tin oxide as stable protective layer for composite cuprous oxide water-splitting photocathodes, Nano Energy. 24 (2016) 10–16. doi:10.1016/j.nanoen.2016.03.022.

[8] J. Luo, M.T. Mayer, M. Grätzel, Perovskite Solar Cells for the Generation of Fuels from Sunlight, in: N. Park, M. Grätzel, T. Miyasaka (Eds.), Org. Halide Perovskite Photovoltaics, Springer International Publishing, 2016: pp. 285–305. doi:10.1007/978-3-319-35114-8_11.

[9] J. Luo, L. Steier, M.-K. Son, M. Schreier, M.T. Mayer, M. Grätzel, Cu2O Nanowire Photocathodes for Efficient and Durable Solar Water Splitting, Nano Lett. 16 (2016) 1848–1857. doi:10.1021/acs.nanolett.5b04929.

[10] J. Luo, D. A. Vermaas, D. Bi, A. Hagfeldt, W. A. Smith, M. Grätzel, Bipolar Membrane Assisted Solar Water Splitting in Optimal pH, Adv. Energy Mater. 2016, 6, 1600100, doi: 10.1002/aenm.201600100.

[11] G. Segev, H. Dotan, K.D. Malviya, A. Kay, M.T. Mayer, M. Grätzel, A. Rothschild, High Solar Flux Concentration Water Splitting with Hematite (α-Fe_2O_3) Photoanodes, Adv. Energy Mater. 6 (2016) 201500817. doi:10.1002/aenm.201500817.

[12] S. Siol, J.C. Hellmann, S.D. Tilley, M. Grätzel, J. Morasch, J. Deuermeier, W. Jaegermann, A. Klein, Band Alignment Engineering at Cu2O/ZnO Heterointerfaces, ACS Appl. Mater. Interfaces. (2016) acsami.6b07325. doi:10.1021/acsami.6b07325.

[13] P. Dias, M. Schreier, S.D. Tilley, J. Luo, J. Azevedo, L. Andrade, D. Bi, A. Hagfeldt, A. Mendes, M. Grätzel, M.T. Mayer, Transparent Cuprous Oxide Photocathode Enabling a Stacked Tandem Cell for Unbiased Water Splitting, Adv. Energy Mater. 5 (2015) 1501537. doi:10.1002/aenm.201501537.

[14] J. Luo, Z. Li, S. Nishiwaki, M. Schreier, M.T. Mayer, P. Cendula, Y.H. Lee, K. Fu, A. Cao, M.K. Nazeeruddin, Y.E. Romanyuk, S. Buecheler, S.D. Tilley, L.H. Wong, A.N. Tiwari, M. Grätzel, Targeting Ideal Dual-Absorber Tandem Water Splitting Using Perovskite Photovoltaics and $CuIn_xGa_{1-x}Se_2$ Photocathodes, Adv. Energy Mater. 5 (2015) 1501520. doi:10.1002/aenm.201501520.

[15] J. Luo, S.D. Tilley, L. Steier, M. Schreier, M.T. Mayer, H.J. Fan, M. Grätzel, Solution Transformation of Cu2O into CuInS2 for Solar Water Splitting, Nano Lett. 15 (2015) 1395–1402. doi:10.1021/nl504746b.

[16] C.G. Morales-Guio, M.T. Mayer, A. Yella, S.D. Tilley, M. Grätzel, X. Hu, An Optically Transparent Iron Nickel Oxide Catalyst for Solar Water Splitting, J. Am. Chem. Soc. 137 (2015) 9927–9936. doi:10.1021/jacs.5b05544.

[17] L. Steier, J. Luo, M. Schreier, M.T. Mayer, T. Sajavaara, M. Grätzel, Low-Temperature Atomic Layer Deposition of Crystalline and Photoactive Ultrathin Hematite Films for Solar Water Splitting, ACS Nano. 9 (2015) 11775–11783. doi:10.1021/acsnano.5b03694.

7 PECHouse3 publications presently under review:

[18] Y. Hu, F. Boudoire, M.T. Mayer, S. Yoon, M. Grätzel, A. Braun, On the function and electronic structure of the SnO2 buffer layer between α-Fe2O3 water oxidation photoelectrode and transparent conducting oxide current collector, ACS Appl. Mater. Interfaces. (2017) under revision.

[19] L. Pan, M. T. Mayer, M-K, Son, A, Ummadisingu, A. Hagfeldt, J. Luo, M. Grätzel, New Benchmark Cu_2O Photocathodes for Solar Water Splitting, Nature Catalysis, under revision.

[20] Y-X. Yu, L. Pan, M-K. Son, M. T. Mayer, W-D, Zhang, A. Hagfeldt, J. Luo, M. Grätzel, Solution Processed Cu_2S Photocathodes for Efficient Solar Water Hydrogen Generation from water Splitting, ACS Energy Letters, submitted.